

STRESS ON THE SAN ANDREAS FAULT:  
AN ANALYSIS OF SHALLOW STRESS RELIEF MEASUREMENTS  
MADE NEAR PALMDALE, CALIFORNIA, 1979 AND 1980

by  
Christopher Edward Flaccus

---

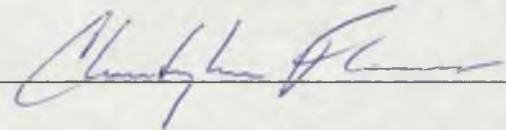
A Thesis Submitted to the Faculty of the  
DEPARTMENT OF GEOSCIENCES  
In Partial Fulfillment of the Requirements  
For the Degree of  
MASTER OF SCIENCE  
In the Graduate College  
THE UNIVERSITY OF ARIZONA

1988

PARCHMENT DEED  
STATEMENT BY AUTHOR  
SOUTHWORTH, GO. U.S.A.

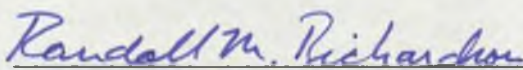
This thesis has been submitted in partial fulfillment of requirements for an advanced degree at the University of Arizona and is deposited in the University Library to be made available to borrowers under the rules of the Library.

Brief quotations from this thesis are allowable without special permission, provided that accurate acknowledgement of source is made. Requests for permission for extended quotations from or reproduction of this manuscript in whole or in part may be granted by the head of the major department or the Dean of the Graduate School when in his judgement the proposed use of the material is in the best interests of scholarship. In all other instances, however, permission must be obtained from the author.

SIGNED: 

## APPROVAL BY THESIS DIRECTOR

This thesis has been approved on the date shown below:



R. M. RICHARDSON

Associate Professor of Geosciences

11 July 1988

/Date

## ACKNOWLEDGMENTS

I would like to thank the members of my thesis committee, Drs. Jaak Daemen and Clement Chase, for their helpful and expedient criticisms of this manuscript. Thanks are also extended to Drs. Marc Sbar and Terry Engelder, two of those who made this research project possible, to Sue Beard and Dr. John Sumner, who subtly prompted me to finish this thing, and to Kathy for her love and reassurance.

Last, but far from least, my sincerest gratitude goes to my advisor Dr. Randall Richardson. Without his enthusiasm, support, patience and positive criticism, I surely never would have done it.

## TABLE OF CONTENTS

	Page
LIST OF ILLUSTRATIONS . . . . .	5
LIST OF TABLES . . . . .	7
ABSTRACT . . . . .	8
1. INTRODUCTION . . . . .	9
2. BACKGROUND . . . . .	13
Technique . . . . .	13
Modulus Determination . . . . .	15
Data Reduction . . . . .	22
Site Descriptions . . . . .	26
Residual and Topographic Stresses . . . . .	30
Thermal Stresses . . . . .	32
Rock Fabric . . . . .	36
3. DATA . . . . .	38
Data Uncertainty . . . . .	43
Moduli . . . . .	45
Sites LRS and TKY . . . . .	45
Site IMS . . . . .	50
Sites ADB and RBT . . . . .	54
4. RESULTS . . . . .	56
Thermal Stresses . . . . .	56
Sites LRS and TKY . . . . .	56
Site IMS . . . . .	65
Sites ADB and RBT . . . . .	68
Tectonic Stress . . . . .	72
5. CONCLUSIONS . . . . .	79
REFERENCES . . . . .	82

## LIST OF ILLUSTRATIONS

Figure	Page
1. Overcoring a U.S. Bureau of Mines stress relief gauge. . . . .	14
2. Typical stress relief curve. . . . .	16
3. Biaxial chamber deformation curves. . . . .	19
4. Deformation during first and second loading cycles in biaxial chamber. . . . .	21
5. Orientations of displacements $U_x$ , and maximum and minimum horizontal compressive stresses P and Q with respect to the borehole. . . . .	24
6. Simplified geologic map of the western Mojave desert near Palmdale, California. . . . .	27
7. Young's moduli versus depth at site LRS. . . . .	46
8. Frequency distribution for axes of maximum Young's moduli at site LRS. . . . .	47
9. Young's moduli versus depth at site IMS. . . . .	52
10. Frequency distribution for axes of maximum Young's moduli at site IMS. . . . .	53
11. Monthly average surface temperatures for the Palmdale, California airport. . . . .	57
12. Horizontal stresses versus depth at sites LRS and TKY. . . . .	59
13. Frequency distribution for P axes at site LRS with $P/Q \geq 1.4$ and depth $> 6m$ . . . . .	62
14. Frequency distribution for P axes at site LRS for depth $\leq 6 m$ . . . . .	63
15. Frequency distribution for P axes at site TKY with ratios of $P/Q \geq 1.4$ , and depth $> 6m$ . . . . .	64

LIST OF ILLUSTRATIONS--Continued

Figure		Page
16.	Horizontal stresses versus depth at site IMS. . . . .	66
17.	Frequency distribution for P axes at site IMS within 6 m of the surface. . . . .	69
18.	Frequency distribution for P axes at site IMS deeper than 6 m. . . . .	70
19.	Horizontal stresses versus depth at sites ADB and RBT. . . . .	71

## LIST OF TABLES

Table	Page
1. Stress data from site LRS . . . . .	39
2. Stress data from site TKY . . . . .	40
3. Stress data from site IMS . . . . .	41
4. Stress data from sites ADB and RBT . . . . .	42

## ABSTRACT

In situ stresses were measured near the San Andreas fault, in the western Mojave desert near Palmdale, California. The U. S. Bureau of Mines stress relief technique was used with boreholes to depths of 29 m. At depths shallower than 6 m, results suggest that both the magnitudes and orientations of maximum horizontal compressive stress are dominated by seasonal ambient temperature variations. Average orientations for the axes of maximum horizontal stress measured below 6 m depth were found to be  $N 16^{\circ} - 26^{\circ} W$ , in agreement with tectonic stress orientations measured by others in the vicinity at much greater depth. This agreement leads to the conclusion that the stresses measured deeper than 6 m are indeed tectonic in origin, and that the U. S. Bureau of Mines stress relief technique can be used as a reliable indicator of regional stress patterns.

CHAPTER 1  
INTRODUCTION

Knowledge of the tectonic stress field associated with an active fault, as inferred from direct measurements of in situ stress states, may be critical to an understanding of fault rheology, strain accumulation and release, earthquake triggering mechanisms, and ultimately earthquake prediction. The San Andreas fault in California, a plate boundary between the Pacific and North American plates, is well suited to attempts at inferring the state of stress near active faults.

Investigations into the stress field surrounding the San Andreas fault have typically relied on one or more experimental techniques used to measure stresses in situ. These include deep hydrofracture techniques (Zoback et al., 1980; 1987; McGarr et al., 1982), vibrating wire continuous stress meters (Clark, 1980), and shallow stress relief techniques (Sbar et al., 1979; 1984; Tullis, 1981). More recently, the orientations of stress-induced wellbore breakouts have been used to infer the state of stress in both petroleum and scientific test wells (Plumb and Hickman, 1985; Zoback et al., 1985; Zoback et al., 1987). Shallow measurements, including both the continuous stress meter and strain relief techniques, have the distinct advantage of being relatively inexpensive. They are,

however, subject to complications which potentially interfere with interpretation of the measured stresses. These are topographic effects which result from the proximity of a site to mountainous terrain (Jaeger and Cook, 1969; Harrison, 1976), and thermal stresses arising from periodic surface temperature variations (Jaeger and Cook, 1969; Hooker and Duvall, 1971; Dahlgren, 1980). In addition, residual stresses locked into the rock from a previous strain history may be significant, regardless of the depth to which measurements are made (Friedman, 1972). While interference from topographic stresses can be minimized through proper site selection, the effects of residual and thermal stresses on measurements may be more difficult to determine. Deep wellbore techniques should be beyond the influence of thermal and topographic effects. Although they might therefore be more reliable than shallow methods, deep measurements are considerably more difficult and expensive to make. Clearly there is a place for an inexpensive, near surface in situ stress technique, provided it can be shown possible to reliably measure tectonic stresses.

With this goal in mind, the U. S. Bureau of Mines strain relief technique has been used to map the stress field in the vicinity of the San Andreas fault near Palmdale, California (Sbar et al., 1979; Dahlgren et al., 1979; Flaccus et al., 1980; Sbar et al., 1984). Data

collected at two sites in 1979, and three sites during 1980, suggest that consistent orientations for the principal stresses can be obtained using this technique, provided measurements are made deeper than 5 to 6 meters. The NNW orientations found for the maximum compressive stresses below this depth are in close agreement with tectonic interpretations by others using methods sensing to much greater depths (Zoback et al., 1979; 1980; 1987; Savage and Gu, 1985; Sbar et al., 1984). Data collected within 6 meters of the surface exhibit markedly different characteristics than data from deeper locations, however. At one site, nearly isotropic stresses near the surface decay approximately exponentially in magnitude with depth to an anisotropic stress field below 6 meters. At another site, near surface stresses are nearly uniaxial with predominantly NNE orientations, while stresses with NNW orientations predominate at depth. These results suggest that both the orientation and magnitude of near surface stresses in certain outcrop settings are dominated by thermal effects, the most significant of which are seasonally-periodic surface temperature fluctuations. Stress magnitudes measured at another site, made during both summer and winter seasons, support this argument.

This thesis presents an analysis of stress data accumulated during 1979 and 1980. The results are compared with those obtained by other investigators, and an attempt

is made to establish the applicability of this near surface technique to the measurement of tectonic stress.

## CHAPTER 2

### BACKGROUND

#### Technique

The U. S. Bureau of Mines stress relief technique is a method used to measure rock stresses in which the deformational response of a sample core is measured as it is freed from its surrounding stress field. The device used in this study consists of a cylindrical stainless steel tool, housing six brass cantilevers, each of which contact the wall of a 3.8 cm diameter borehole in a rock outcrop. The cantilevers are oriented at  $60^{\circ}$  from one another. An electrical resistance strain gauge is bonded to each cantilever, and monitors the bending moment of its respective arm as a function of the electrical resistance of the gauge. Temperature fluctuations in the tool are compensated for by six additional unstressed gauges within the housing, which act as comparison for the D. C. balance bridge used to measure active gauge resistance (Hooker and Duvall, 1974). In this manner, diametrical deformations of an initially circular borehole can be accurately monitored while the tool is concentrically overcored using a larger diameter drill bit. Figure 1 shows the U. S. Bureau of Mines strain gauge during the overcore process. A complete description of the theory and operation of this gauge may be found in a series of U. S. Bureau of Mines reports

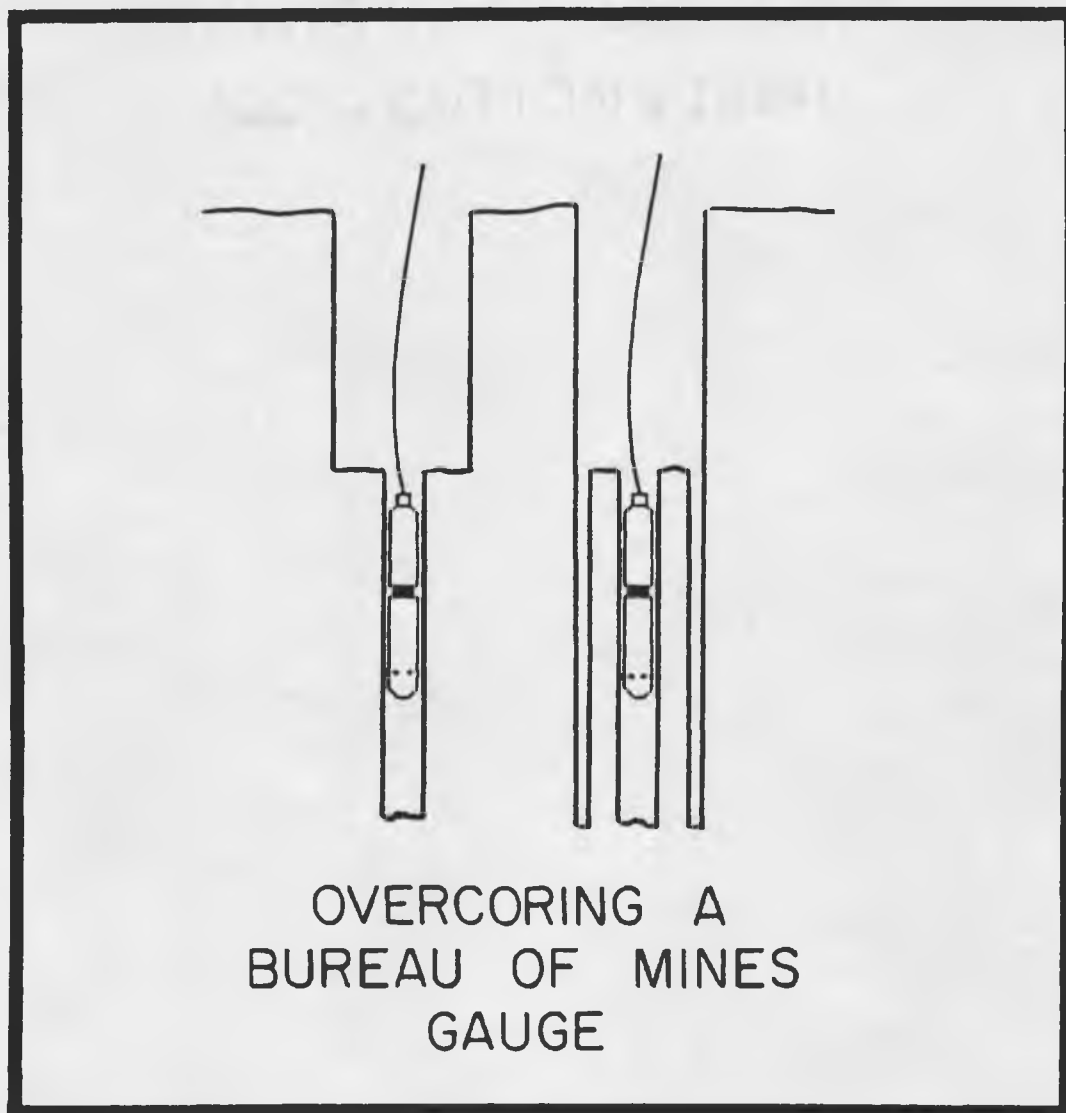


Figure 1. Overcoring a U.S. Bureau of Mines stress relief gauge.

(Merrill and Peterson, 1961; Obert, 1962; Merrill, 1967; Hooker and Bickel, 1974).

For our field determination of rock stresses, the tool is first oriented azimuthally at depth within a vertical borehole in the rock outcrop. The gauge is then concentrically overcored with a 14.3 cm inner diameter bit while the deformation of the 3.8 cm borehole is recorded. Figure 2 shows a typical strain relief curve obtained while coring a relatively compliant sandstone. The slight compression of each component immediately preceding relaxation represents the response of the rock to the bit passing the gauge. Because minute adjustments of the gauge within the borehole are inevitable after placement (due to changes in drilling fluid pressure, etc.), the total deformation along each component is determined relative to the value observed just prior to this deformation peak. The net positive change observed in Figure 2 indicates an expansion of the core segment in response to the release of compressive stress during the overcore process.

#### Modulus Determination

Borehole deformation data can be used to estimate the horizontal state of stress in an outcrop provided the elastic moduli of the rock are known. To minimize the effects of heterogeneity, these moduli are determined for each measurement location after the core is removed from

LRS 19.38 m

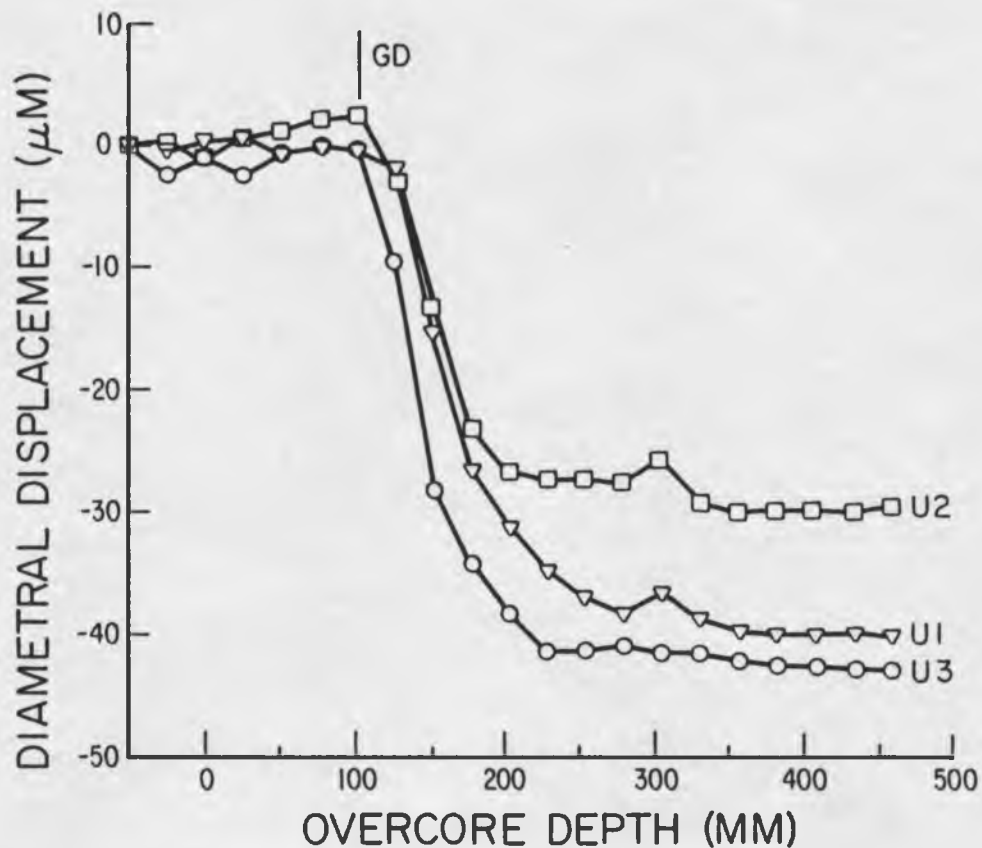
AZIMUTH  $U_1 = -86^\circ$ 

Figure 2. Typical strain relief curve. The sample shown is from relatively compliant sandstone at site LRS. Diametrical displacements are shown plotted vs. depth of the core barrel. GD refers to the gauge depth during overcoring, in this case 19.38 m. The azimuth of  $U_1$ , as oriented in the borehole, is shown at the top of the figure.

the ground. The gauge is first re-oriented at a measurement location within a core segment. The cylindrical core is then subjected to a uniform biaxial stress over 25 cm of its length while the borehole diameters are again monitored. Deformation is recorded with increasing pressure until strain values approximately equal to those observed in the field are achieved. The pressure is then decreased to zero, resulting in a complete cycle of loading and unloading deformation. In addition to measuring an average Young's modulus for a given core segment, any horizontal anisotropy in the rock's compressibility is also determined by this process.

Determination of modulus anisotropy from biaxial chamber data is approximate because conditions are not the same as those found in situ. The ends of a core segment are unconfined to axial strain, and only a small sample area is stressed by the biaxial chamber. Furthermore, one cannot determine Poisson's ratio using this technique. As a consequence, an exact solution for in situ rock stresses is not possible. An approximate method for data reduction was shown by Tullis (1981) to yield results consistent with a more involved orthotropic approximation of rock properties, however. In this method, three "effective" Young's moduli are estimated for each core segment by assuming that the equation for the modulus of a uniformly stressed, isotropic thick walled cylinder applies to the deformation

of each component observed during biaxial testing. That is,

$$E_i = 2dD^2P_o / (D^2 - d^2)U_i ; \quad (1)$$

where  $E_i$  and  $U_i$  are the effective modulus and deformation along component  $i$ ,  $d$  and  $D$  are the inner and outer diameters of the cylinder, and  $P_o$  is the uniformly applied external pressure (Saada, 1974).

Significant non-linearity in stress-strain relations was observed in our determination of rock moduli. In addition, considerable hysteresis was encountered when the core was unloaded to zero pressure, particularly with the soft sandstone encountered at one site. Figure 3 shows examples of these phenomena for two of the rock types tested in this study.

Non-linear rock behavior is described by Walsh (1965), and Jaeger and Cook (1969) as representing various stages of microcrack closure within the rock matrix during compression. Consider the stress-deformation curve of the sandstone in Figure 3. The steep segments of this curve, near the beginning of both the loading and unloading portions of the cycle, approach a higher "intrinsic" modulus of the sample core. It is unclear why this high modulus would be observed at very low stresses. At larger stresses, however, the phenomenon is more understandable.

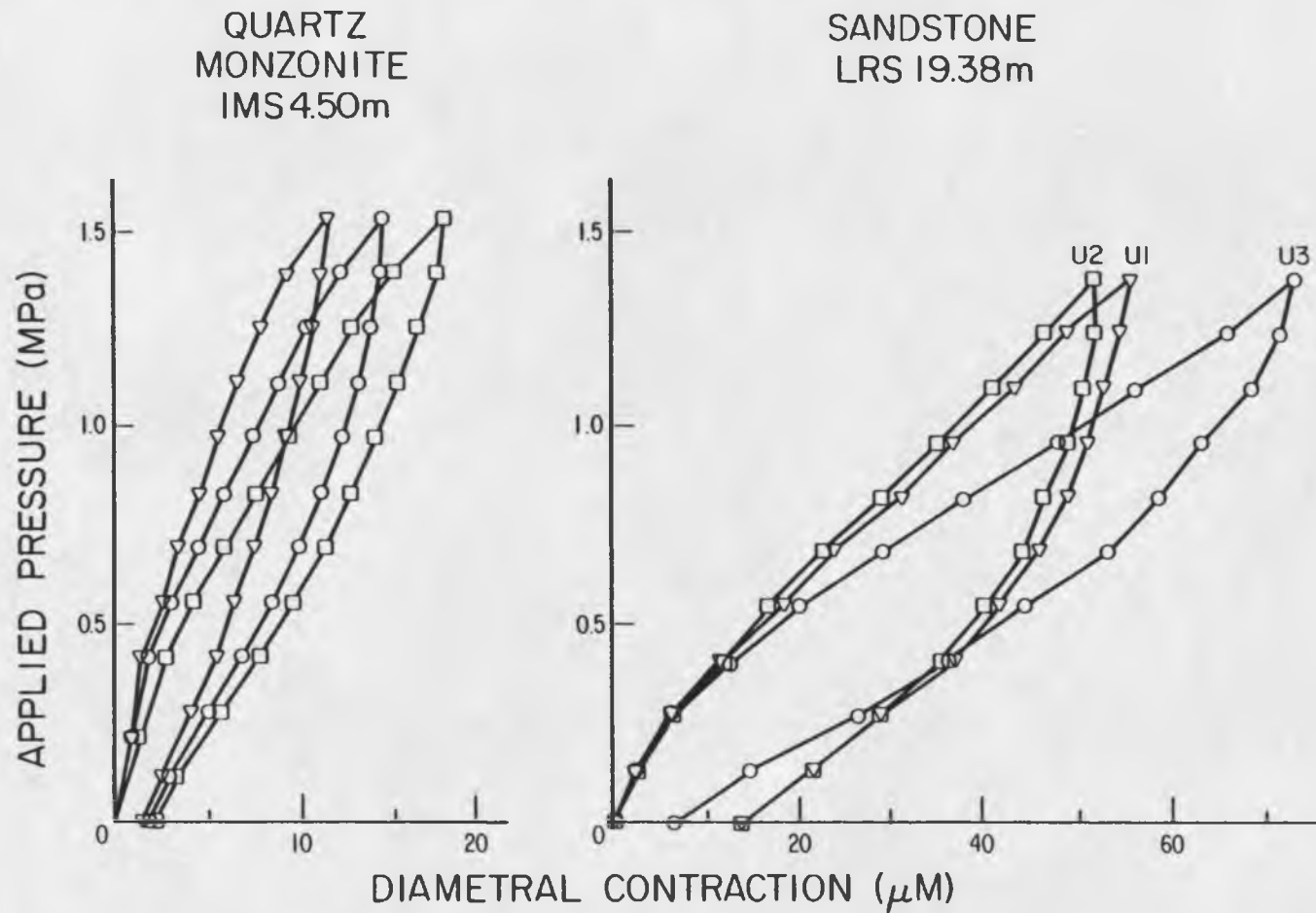


Figure 3. Biaxial chamber deformation curves. Coordinate axes are the same as in Figure 2. Moduli are determined using the unloading portion of the cycle. Both non-linearity and hysteresis are more pronounced in the sandstone at site LRS than in the monzonite at site IMS.

As stress on the core is increased, microcracks within the core apparently begin to close, and a low "effective" modulus is observed. When confining pressures are sufficient to have closed these microcracks, a higher "intrinsic" modulus is approached, near the maximum stress applied to the core. The process is approximately the same during decompression, with an "intrinsic" modulus observed near the beginning of the unloading portion of the cycle.

The hysteresis observed in sandstone samples (Figure 3), implies that either a permanent strain occurs in a core sample during biaxial testing, or relaxation is time dependent and not fully monitored. No core segments were monitored over a long enough period to test time dependency. Some core segments were, however, subjected to two cycles of pressurization. As shown in Figure 4, during a second cycle the maximum deformation for a given maximum stress is regained, while no hysteresis is observed when the core is returned to zero pressure. The same results were obtained for the monzonite samples tested, although first cycle hysteresis observed is much smaller. These results appear to indicate that the hysteresis results from a time dependent relaxation which is not fully monitored during the first cycle. Permanent strain resulting from the relatively low stresses of a biaxial chamber test seems unlikely.

Both hysteresis and non-linear behavior observed

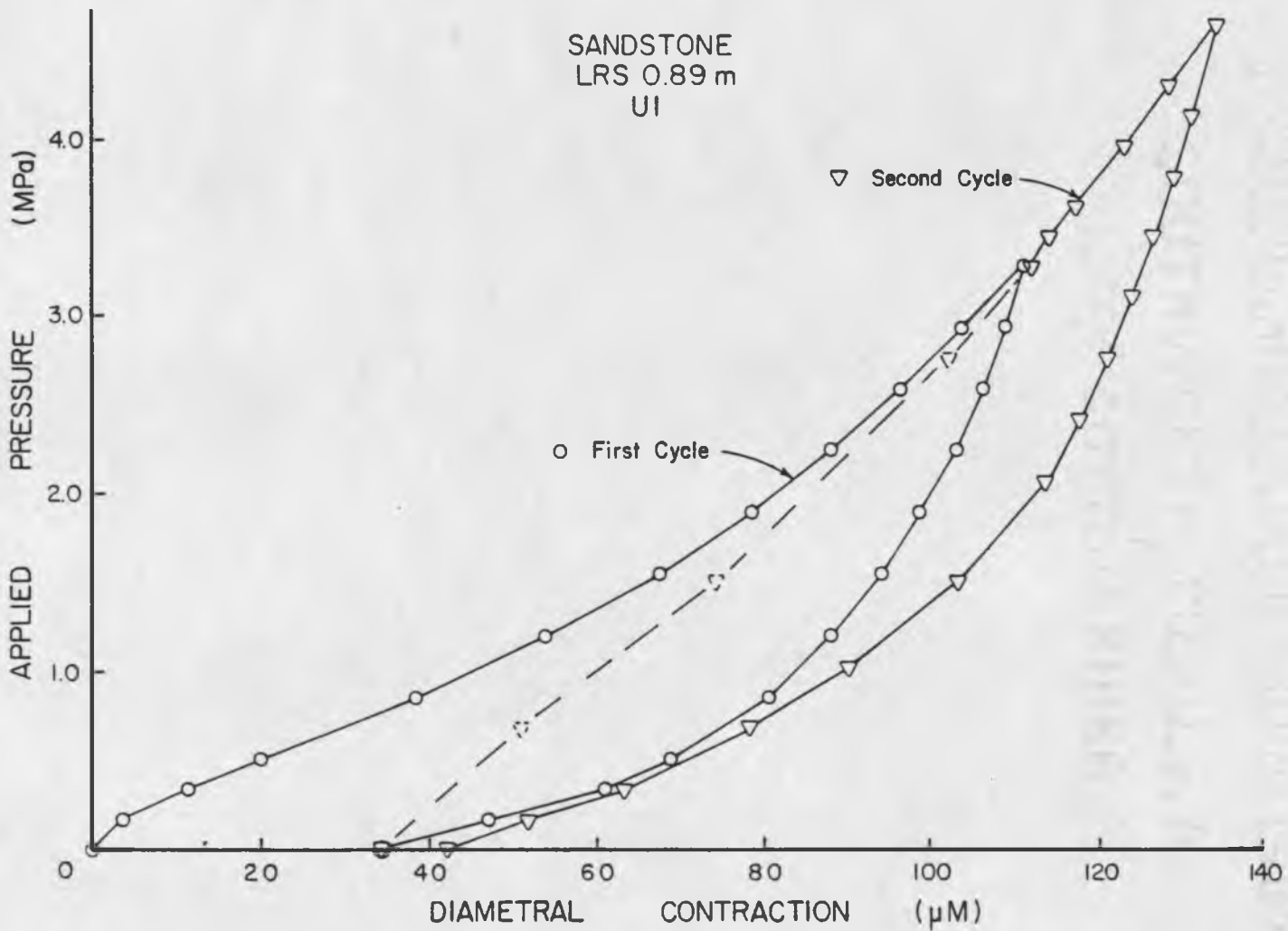


Figure 4. Deformation during the first and second loading cycles in a biaxial chamber. Only one component of borehole deformation is shown. Hysteresis during second cycle is much less pronounced than during first cycle.

during this study lead to questions about the appropriate calculation for rock compressibility. As much as possible, conditions within the biaxial chamber were matched to the respective measurement. Because deformation in the field is measured as the rock is depressurized, secant moduli have been calculated from biaxial test data while unloading the core to zero pressure (Tullis, 1981; Sbar et al., 1984). Furthermore, each segment was tested at approximately the same rate of speed at which the original measurement was made. It is assumed that an "effective" modulus determined in this manner is appropriate for this technique, and minimizes the effects of inelastic and non-linear rock behavior on moduli and thus stress calculations.

#### Data Reduction

With estimates of rock anisotropy and moduli, one can infer the state of stress in the rock outcrop from diametrical deformations measured during overcoring. To accomplish this, each effective modulus is used to modify its respective displacement using the relation

$$U_i^m = [E_i / \langle E \rangle] U_i, \quad (2)$$

where  $U_i^m$  are modified displacements, and  $\langle E \rangle$  is the average of the three  $E_i$ . This corrects each component by

reducing deformation in directions having small moduli, while increasing deformation in directions having larger moduli (Tullis, 1981). Using modified displacements and an average modulus for a given core location, the state of stress in the plane perpendicular to the borehole can be estimated. This is accomplished by using the equations for a circular hole in an isotropic material under a plane strain state of stress (Merrill and Peterson, 1961).

$$P = \langle E \rangle (R + S) / 6d(1 - \nu^2) \quad (3)$$

$$Q = \langle E \rangle (R - S) / 6d(1 - \nu^2) \quad (4)$$

$$\theta = 1/2 \tan^{-1} \{ \sqrt{3} (U_3^m - U_2^m) / (2U_1^m - U_2^m - U_3^m) \} \quad (5)$$

Where: P = maximum horizontal principal stress,

Q = Minimum horizontal principal stress,

$\theta$  = angle from  $U_1$  to P (positive direction is clockwise),

$$R = U_1^m + U_2^m + U_3^m,$$

$$S = (\sqrt{2}/2) [(U_1^m - U_2^m)^2 + (U_2^m - U_3^m)^2 + (U_3^m - U_1^m)^2]^{1/2},$$

$\nu$  = Poisson's ratio.

These equations describe the orientation and magnitude of the principal axes of a horizontal stress ellipse, presuming that the third principal stress is aligned with the vertical borehole. The orientations of these parameters with respect to a deformed borehole are depicted in

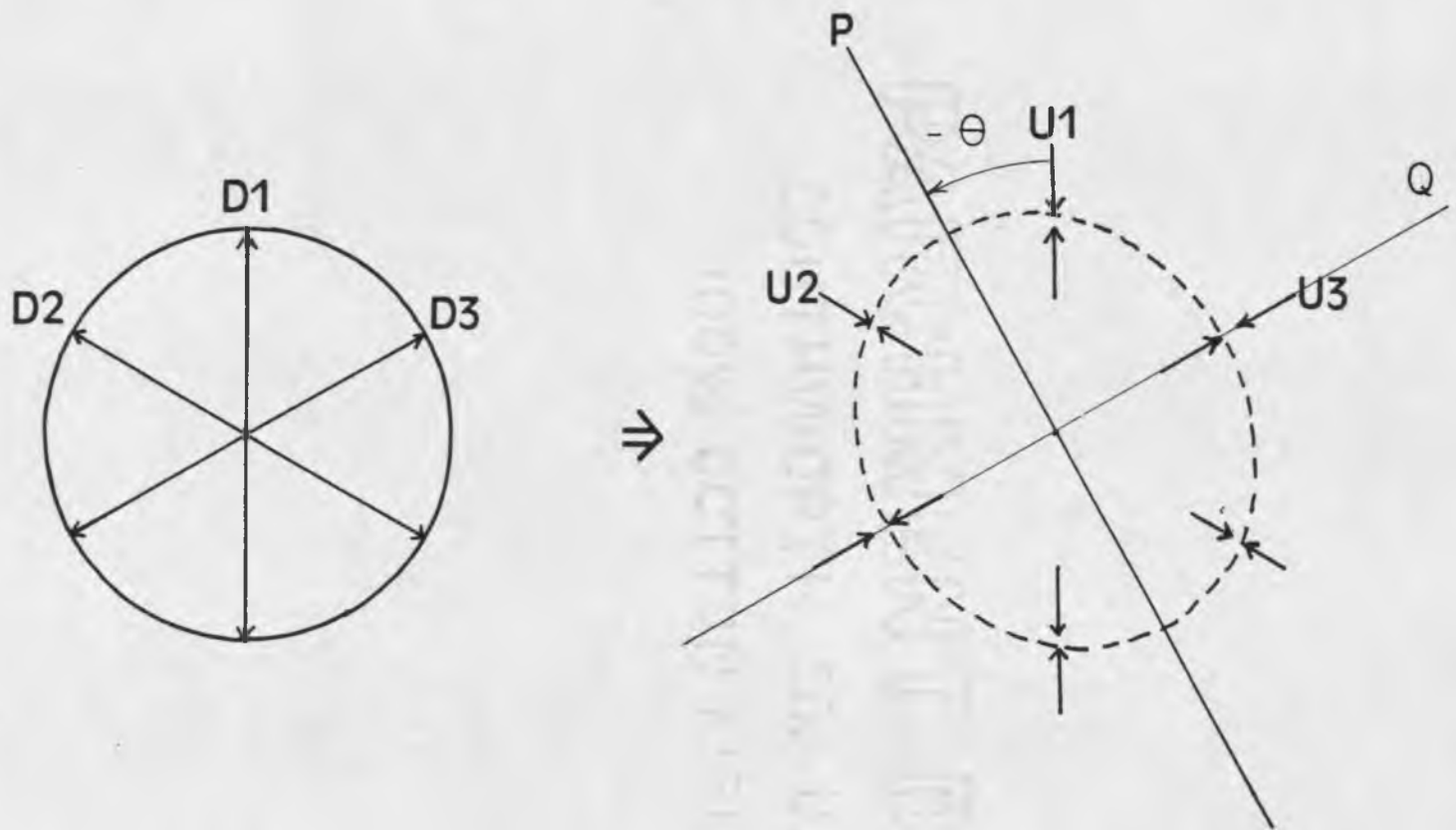


Figure 5. Orientations of displacements  $U_i$ , and maximum and minimum horizontal compressive stresses P and Q, respectively, with respect to the borehole (Hooker and Bickell, 1974).

Figure 5.

Data can also be reduced assuming a plane stress state. The resulting equations for P and Q are

$$P = \langle E \rangle (R+S)/6d, \quad (6)$$

$$Q = \langle E \rangle (R-S)/6d. \quad (7)$$

The orientations of P and Q remain unchanged from the plane strain approximation (Merrill and Peterson, 1961).

It is unclear whether a plane strain or plane stress state is most appropriate for the outcrop during overcoring (Tullis, 1981). Measurements made very close to the free surface, where there is very little vertical stress, are likely to experience plane stress deformation. Deeper measurements might be presumed to be in a plane strain state because of the effect of lithostatic load. The core, however, is axially unconfined as it is released from surrounding rock. Vertical strains within the core cannot be measured with a gauge of this type, therefore the true state remains an unknown. The two approximations may represent extremes between which stress values would lie. Calculations have been made using both approximations at both sites using assumed values for Poisson's ratio. The magnitudes of P and Q were found to differ by less than 19% between the two cases.

### Site Descriptions

A detailed description of the regional geology of the western Mojave Desert northeast of Palmdale is given by Dibblee (1967), and is shown in simplified map form in Figure 6. He describes the local setting as typical of the broad desert basin topography of the Mojave block lying to the northeast of the San Andreas fault. Bedrock consists of Mesozoic granites and quartz monzonites which occasionally protrude through an alluvial plain. These low lying buttes usually contain large blocks of material which are highly fractured. Bounding the Mojave to the south and west is the San Andreas fault, and beyond that the San Gabriel Mountains. The San Gabriel Mountains are a rugged terrain consisting of primarily sedimentary and metamorphic rocks, in complicated assemblages of dioritic gneisses, shaley sandstones and sandstone conglomerates. The dominant structural trend in this area lies sub-parallel to the San Andreas fault, which strikes N 65° W.

Two sites, IMS and LRS, were occupied during the summer of 1980. In addition, data were reinterpreted from sites TKY, ADB and RBT, occupied during previous field seasons. All sites are shown on the geological map of the area in Figure 6. Also shown are sites XTLR, MOJ1, MOJ2 and BB, all deep wells in the vicinity in which hydrofracture measurements have been made (Zoback et al., 1980; Stock et al., 1986).

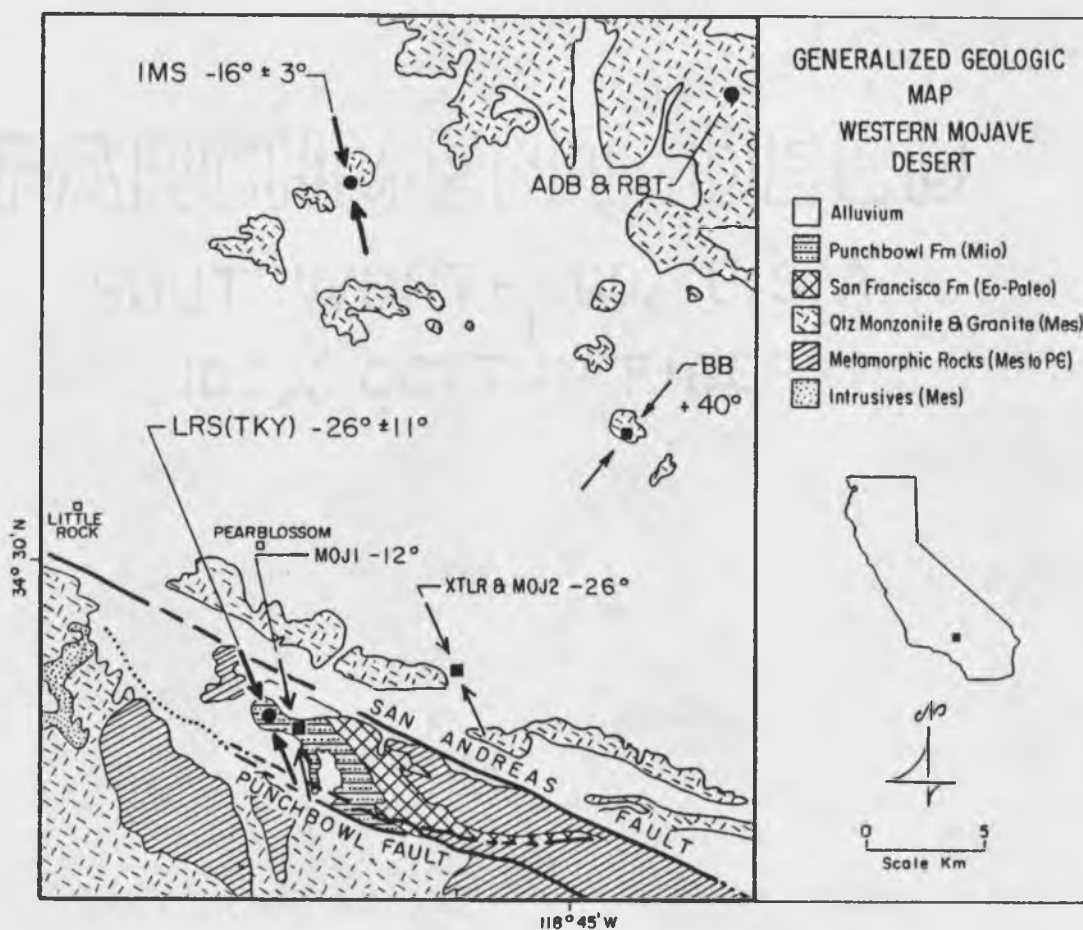


Figure 6. Simplified geologic map of the western Mojave desert near Palmdale, California (Dibblee, 1967). Sites occupied during the course of this study are IMS, LRS, ADB and RBT. Deep hydrofracture measurements by others in the vicinity are denoted by MOJ1, MOJ2 and XTLR (Zoback et al., 1980), and BB (Stock et al., 1986).

Site IMS was located on the relatively level southern arm of Piute Butte in a Mesozoic quartz monzonite, about 20 km northeast of the San Andreas fault. At the surface, outcrop fractures were observed to have a spacing of 1 to 3 m, with a predominant strike of  $N 40^{\circ} E$  and near vertical dip. In the vicinity of the 30 m borehole however, a densely fractured rock with a typical spacing of 5 to 19 cm was encountered to a depth of 13 m. Between 6 m and 13 m depth, the rock was so incompetent that drilling was extremely difficult and it was not possible to make any measurements. Below this depth fractures were observed to have predominant strikes and dips of  $N50^{\circ}W$   $56^{\circ}NE$ ,  $N60^{\circ}W$   $55^{\circ}SW$ , and horizontal. Those fractures within 13 m of the surface were generally open and deeply weathered as evidenced by mineralization on the fragments recovered. Fractures encountered below this depth were typically closed and less deeply weathered. Sixteen successful stress measurements were made at this site, to a total depth of 28.6 m.

Site LRS was located in an outcrop of sandstone conglomerate in the Miocene Punchbowl Formation, approximately 2 km southwest of the San Andreas fault. Locally this rock is a poorly sorted, medium to coarse grained and thickly bedded arkosic sandstone that is moderately indurated. Silty sandstones were found to alternate with bands of pebble conglomerate. Clasts of up to 2 cm in

diameter are common in the conglomerate, generally consisting of gneiss, granite and schist, apparently from surrounding formations in the San Gabriel Mountains. The outcrop sampled is located at an elevation of 1300 m on the northern limb of a synclinal fold which plunges  $30^{\circ}$  toward the WNW. Locally, the strike and dip of bedding was  $N50^{\circ}W$   $50^{\circ}SW$ , and the outcrop found to be nearly free of fractures. Only a single bedding plane fracture was observed in the entire 28 m core sampled. Due to the consistency of this rock, technical problems were minimal and measurements were extremely easy to make. Forty successful stress measurements were made at site LRS.

Site TKY, occupied during July of 1979, is located on the same outcrop as LRS, approximately 10 m away. Fifteen measurements were made to a total depth of 11 m at this location, and the core found to have similar characteristics to that at LRS (Dahlgren, 1980).

Sites ADB and RBT were occupied during June, 1979 and January, 1980, respectively. These sites are 5 m apart on an outcrop of Mesozoic granite, approximately 35 km northeast of the San Andreas fault. This rock is medium to fine grained, and highly fractured. Coarsely grained pegmatitic dikes and fracture spacings of 3 cm to 2 m were encountered within the borehole. Fracture orientations were found to strike E-W, N-S, and  $N.45^{\circ}E$ , all with steep dips (Dahlgren, 1980). Four measurements were made during

the summer at ADB, to a depth of 4 m. Eight measurements were made during the winter at RBT, to a depth of 8 m.

### Residual and Topographic Stresses

Sites LRS and TKY lie approximately 3.5 km from the N65°W striking San Gabriel Mountain front, where peaks locally rise to 2400 m. This vertical relief is enough to cause suspicion of significant topographic stresses. For an isotropically applied regional stress field, one would expect the San Gabriels to reduce the strain component perpendicular to the strike of the mountain front. Using the finite element model of Harrison (1976), the ratio of strain perpendicular to strike to strain parallel to strike at this distance from the mountain range is predicted to be approximately 0.95. If this model is correct, we expect to measure anisotropy in a uniformly applied isotropic stress field at this site; the P axis inferred would be oriented N65°W, with a ratio  $P/Q = 1.05$ . This difference in the relative magnitudes of P and Q is too small to resolve with the type of strain relief equipment used in this study, and thus topographic effects have been neglected at this site.

At sites IMS and ADB (RBT), the surrounding relief, less than 120 m, is low enough that topographic stresses due to the buttes themselves are negligible. Basement topography beneath the alluvium could be significant however, as evidenced by the gravity data of Mabey (1960).

He has interpreted these two buttes as lying atop adjacent, northeasterly trending, basement highs. Harrison (1976) predicts a reduction of stress, perpendicular to strike, for points atop a ridge feature in an isotropically applied stress field. The northeast trending basement ridges below these sites might therefore generate a topographic stress field with the axis of maximum compressive stress oriented NE. Basement topography at these sites is not sufficiently known to make predictions about the importance of this effect. Comparison of stress data collected during this study, to those of other investigators measuring to greater depths, does suggest that topographic stresses are negligible here as well (Zoback et al., 1980).

Residual stresses were found to be negligible at sites LRS and ADB by Sbar et al. (1979), using a double overcore technique with a "doorstopper" strain gauge. In this technique, a three component strain gauge is bonded directly to the rock at the bottom of a shallow 3.8 cm diameter borehole. The gauge is then overcored with a 23 cm diameter bit while rock strains are monitored in similar fashion to the U. S. Bureau of Mines technique. After external stresses on the core have been relieved, the gauge is overcored a second time with a smaller, 14.3 cm diameter bit while rock strains are again monitored. In this manner, internal stresses in the rock will hopefully be monitored during the second overcore. No double overcores

were done at site IMS, the assumption being made that residual stresses would be negligible there as they were at the other sites.

### Thermal Stresses

Thermal strains and/or stresses arise in a body when it is heated or cooled from its ambient stress-free temperature. In general, a thermoelastic, isotropic material will experience no shear strains if the object if it is allowed to expand or contract uniformly in all directions (Boley and Weiner, 1960). For an isotropic solid, therefore, expansion or contraction results in three equal thermal strains ( $e_{ii}^t$ ) along the coordinate axes, each proportional to the temperature change ( $\Delta T$ ) of the material:

$$e_{xx}^t = e_{yy}^t = e_{zz}^t = \alpha \Delta T \quad (8)$$

where  $\alpha$  is the coefficient of thermal expansion for the isotropic material, and  $x$ ,  $y$  and  $z$  refer to a cartesian coordinate system. These thermal strains can be added to those defined by Hooke's Law for a linearly elastic, isotropic solid to obtain a complete thermoelastic stress-strain relationship. The resulting expressions for the total strain in the solid are:

$$e_{xx} = (1/E)[\sigma_{xx} - \nu(\sigma_{yy} + \sigma_{zz})] + \alpha \Delta T \quad (9)$$

$$e_{yy} = (1/E)[\sigma_{yy} - v(\sigma_{zz} + \sigma_{xx})] + \alpha\Delta T \quad (10)$$

$$e_{zz} = (1/E)[\sigma_{zz} - v(\sigma_{xx} + \sigma_{yy})] + \alpha\Delta T \quad (11)$$

$$e_{xy} = \sigma_{xy}/2u \quad (12)$$

$$e_{xz} = \sigma_{xz}/2u \quad (13)$$

$$e_{yz} = \sigma_{yz}/2u \quad (14)$$

where  $e_{ij}$  and  $\sigma_{ij}$  refer to the tensor shear components,  $E$  is Young's modulus,  $v$  is Poisson's ratio and  $u=E/(2(1+v))$  is the shear modulus for the material.

Consider a laterally confined rock outcrop in which horizontal  $(x,y)$  expansions due to temperature changes are restricted, but vertical strains are unconfined. In the absence of externally applied stresses, the strains in the rock are  $e_{yy} = e_{xx} = e_{xy} = e_{xz} = e_{yz} = 0$ . From equations 12 - 14,  $\sigma_{xz} = \sigma_{yz} = 0$ . At the surface of the outcrop, a stress free boundary condition requires that  $\sigma_{zz} = 0$ . If vertical stresses due to lithostatic loading are neglected near the surface, solution of equations 9 and 10 yields:

$$\sigma_{xxt} = \sigma_{yyt} = E \alpha\Delta T/(1-v), \quad (15)$$

where  $\sigma_{xxt}$  and  $\sigma_{yyt}$  are horizontal stresses within the outcrop due to changes in its temperature.

Both seasonal and diurnal surface temperature fluctuations have been shown to produce significant stress variations in granite quarries in Texas and North Carolina

(Hooker and Duvall, 1971). In order to investigate the expected thermal stress distribution within a rock mass due to these time varying expansions and contractions, it is necessary to solve for the temperature distribution of the outcrop. An outcrop can be modeled analytically as a semi-infinite, isotropic thermal conductor using the one dimensional conduction equation,

$$T(t,z)/\delta t = k \delta^2 T(t,z)/\delta z^2, \quad (16)$$

where  $T$  is temperature,  $z$  is distance into the solid,  $t$  is time, and  $k$  is the thermal diffusivity of the material. Seasonal and diurnal ambient temperature variations are typically of the form

$$T = T_0 + A \cos(\omega t + \phi), \quad (17)$$

where  $T_0$  is the mean temperature,  $A$  and  $\omega$  are the amplitude and angular frequency of the variation, and  $\phi$  is an arbitrary phase angle. If the surface of the outcrop is subjected to this temperature function, the steady state solution of equation 16 is given by (Carslaw and Jaeger, 1959):

$$T_s = T_0 + A e^{-Kz} \cos(\omega t - Kz + \phi), \quad (18)$$

where  $K = \sqrt{w/2k}$  is the wave number. Equation 18 represents a damped temperature wave about the mean annual surface temperature of  $T_0$ , as a function of both depth and time. The temperature fluctuation is damped to near zero at the characteristic depth for the outcrop,  $z = 1/\sqrt{w/2k}$ . For most rocks undergoing seasonal temperature variations, this depth is about 6 to 15 m. Diurnal variations in temperature only penetrate to a depth of approximately 0.5 m.

If  $T_0$  is assumed to be the stress-free temperature of the rock, the time varying temperature distribution will generate corresponding isotropic horizontal stresses by equation 15, provided the outcrop is unfractured and laterally extensive. The depth to which thermal stress fluctuations are significant depends on the amplitude and the period of the temperature variation, as well as the thermoelastic properties of the rock type. In North Carolina, Hooker and Duvall (1971) measured significant diurnal temperature variations in granite to a depth of 60 cm, while annual variations were reported to a depth of 7.6 m. They measured corresponding rock stresses using the U. S. Bureau of Mines strain relief technique. Surface stress fluctuations of 4.1 MPa due to these daily variations were reported, decaying to 0.1 MPa at a depth of 50 cm. Maximum surface stresses of 4.6 MPa due to seasonal temperature variations were shown to decay to 0.4 MPa at a depth of 7.6 m. Rock properties of  $k = 0.013 \text{ cm}^2/\text{sec}$ ,  $\alpha = 8.1 \times$

$10^{-6}/^{\circ}\text{C}$ ,  $E=30.8$  GPa, and  $\nu=0.11$  were determined for samples of the North Carolina granite, and stress measurements were shown to be in agreement with values predicted by equations 8 and 11.

Hooker and Duvall (1971) measured stresses that were periodic, and superimposed on a relatively high background stress of 18.9 MPa. No change in orientation of the principal stress directions was observed with temperature, indicating that rock behavior was probably thermo-elastically isotropic. Maximum thermal stresses were less than 25% of the background stress observed by the authors in North Carolina. Thermal stresses may present a more significant interference in locations where ambient stresses are low. They may also be more significant in locales where the amplitude of surface temperature variations is large, or where the coefficient of thermal expansion is large.

#### Rock Fabric

The presence of fractures can affect thermal stresses in a rock outcrop in at least three ways. First, open fractures will allow free expansion of the rock in a direction perpendicular to the fracture plane, thereby reducing any stress buildup in this direction. An outcrop of closely spaced joints might therefore produce a uniaxial thermal stress field parallel to fracture strike. Second,

microfractures within the rock fabric are likely to result in anisotropic coefficients of thermal expansion, and hence an anisotropic stress field. Finally, microfractures are also likely to result in anisotropic elastic moduli. In addition to these effects, any residual elastic strain existing in rock grains from a previous tectonic event might also result in anisotropic behavior. As a consequence, equations 15 and 18 represent at best idealized expressions of a thermal stress field in situ. Any attempt to gain information regarding tectonic stresses from measurements made within this thermal zone needs to consider these effects.

## CHAPTER 3

## DATA

Stress and modulus data from sites LRS, TKY and IMS are summarized in Tables 1 through 3, respectively. Results obtained at sites ADB and RBT are combined in Table 4.

Stresses were calculated using both plane stress and plane strain assumptions. Values of 0.20 and 0.40 were assumed for Poisson's ratio for the quartz monzonite at site IMS, and the relatively soft sandstone at site LRS, respectively. These assumptions produced plane strain magnitudes 19% larger than plane stress values at site LRS, while at site IMS the difference is 4%. These 4% differences are likely to be comparable between sites IMS, ADB and RBT. In all cases, the stresses reported in Tables 1 through 4 are plane stress values.

Average orientations reported in this study were calculated using the circular mean and standard deviation developed for axial data by Mardia (1972). Data were grouped in frequency distributions, in which the range ( $-90^{\circ}$  to  $+90^{\circ}$ ) was divided into equal class intervals. Class interval size depended on the total number of observations, and the dispersion within a group of data.

TABLE 1: Stress Data from Site LRS

Depth	Max Horiz Displ	Min Horiz Displ	Azimuth of Max Displ	Max Modulus	Min Modulus	Azim of Max Modulus	Ratio	Max Horiz Stress [Plane Stress]	Min Horiz Stress	Azim of Max Stress	Ratio
m	um	um	E of N	GPa	GPa	E of N	E <sub>max</sub> /E <sub>min</sub>	MPa	MPa	E of N	P/Q
0.89	100.7	90.5	-82	3.40	3.35	53	1.01	4.4	4.1	-87	1.1
1.93	42.1	28.1	-72	6.55	5.13	-32	1.28	3.1	2.4	-58	1.3
2.51	83.2	45.7	-72	2.85	2.29	-6	1.24	2.4	1.9	-63	1.3
2.95 *	63.4	52.1	23	4.18	4.18	nv	1.00	3.3	3.0	23	1.1
3.30	88.4	65.8	64	2.70	2.14	-65	1.26	2.6	2.3	86	1.2
4.04 *	42.5	33.5	57	4.18	4.18	nv	1.00	2.2	2.0	57	1.1
4.45 *	42.0	22.5	-45	4.18	4.18	nv	1.00	2.0	1.5	-45	1.4
4.85 *	43.4	17.5	-51	4.18	4.18	nv	1.00	2.0	1.3	-51	1.5
6.55 *	26.6	6.1	-39	4.18	4.18	nv	1.00	1.2	0.6	-39	1.9
6.96 *	24.2	15.8	-47	4.18	4.18	nv	1.00	1.2	1.1	-47	1.2
7.37	31.3	0.0	-38	5.26	3.26	52	1.61	1.1	0.4	-35	2.9
8.10	32.3	12.4	-22	3.80	3.50	-56	1.09	1.3	0.8	-24	1.6
8.53	19.6	9.0	-28	5.20	4.80	69	1.08	1.1	0.8	-29	1.4
9.09	18.8	5.7	-30	5.11	4.82	7	1.06	1.0	0.6	-28	1.7
9.53	31.1	-3.7	-16	10.29	6.42	-70	1.60	2.3	0.6	-24	3.7
10.06	17.6	11.8	-70	6.71	6.13	34	1.09	1.3	1.1	-74	1.2
10.54	20.9	13.3	-64	4.41	3.72	-53	1.18	1.1	0.8	-61	1.4
11.43	22.5	13.7	51	5.42	4.23	-37	1.28	1.2	1.1	46	1.1
12.12	31.0	17.4	-13	4.67	3.55	18	1.31	1.6	1.1	-3	1.5
12.37 *	24.0	9.3	-86	4.18	4.18	nv	1.00	1.1	0.7	-86	1.6
13.26 *	31.8	27.2	-1	4.18	4.18	nv	1.00	1.7	1.6	-1	1.1
14.91	21.4	15.4	-75	3.32	3.12	71	1.06	0.9	0.7	-79	1.2
15.32	29.2	18.3	47	4.75	4.02	9	1.18	1.5	1.2	38	1.3
15.72	30.1	12.8	-28	3.04	2.98	-81	1.02	1.0	0.7	-29	1.5
16.81 *	34.7	13.3	-2	4.18	4.18	nv	1.00	1.6	1.0	-2	1.6
17.25 *	28.4	22.8	-47	4.18	4.18	nv	1.00	1.5	1.3	-47	1.1
17.78 *	26.5	20.1	75	4.18	4.18	nv	1.00	1.4	1.2	75	1.2
18.57 *	26.7	20.7	-49	4.18	4.18	nv	1.00	1.4	1.2	-49	1.1
18.97	28.4	20.9	88	3.60	2.52	-46	1.43	1.1	0.9	-66	1.3
19.38	46.2	35.7	29	3.69	1.36	60	2.71	1.7	1.0	56	1.7
21.03 *	27.3	3.8	-78	4.18	4.18	nv	1.00	1.2	0.5	-78	2.2
21.51 *	15.1	-1.1	85	4.18	4.18	nv	1.00	0.6	0.2	85	3.6
22.40	32.6	17.7	-39	3.20	2.78	60	1.15	1.1	0.9	-41	1.3
22.91 *	34.1	18.8	-27	4.18	4.18	nv	1.00	1.7	1.2	-27	1.3
23.37	36.7	19.9	-16	4.71	3.57	88	1.32	1.7	1.4	-29	1.2
24.16 *	32.4	-3.4	-38	4.18	4.18	nv	1.00	1.2	1.1	-38	1.2
24.56 *	35.4	-5.4	-13	4.18	4.18	nv	1.00	1.5	0.8	-13	2.0
25.88 *	42.9	22.9	-10	4.18	4.18	nv	1.00	2.1	1.5	-10	1.4
26.34	31.9	11.0	-37	4.92	4.07	23	1.21	1.5	1.0	-30	1.6
27.58 *	73.4	38.6	28	4.18	4.18	nv	1.00	3.6	2.6	28	1.4

TABLE 2: Stress Data From Site TKY

Depth	Max Horiz Displ	Min Horiz Displ	Azimuth of Max Displ	Max Modulus	Min Modulus	Azim of Max Modulus	Ratio	Max Horiz Stress [Plane Stress]	Min Horiz Stress	Azim of Max Stress	Ratio
m	um	um	E of N	GPa	GPa	E of N	E <sub>max</sub> /E <sub>min</sub>	MPa	MPa	E of N	P/Q
0.84 *	88.7	43.5	7	2.7	2.7	nv	1	2.8	1.9	7	1.4
1.40 *	86.6	79.8	0	2.7	2.7	nv	1	3.0	2.9	0	1.0
1.98 *	99.2	55.0	88	2.7	2.7	nv	1	3.1	2.3	88	1.3
2.59 *	85.6	51.9	-26	2.7	2.7	nv	1	2.8	2.1	-26	1.3
4.95 *	31.7	16.3	-19	2.7	2.7	nv	1	1.0	0.7	-19	1.4
5.69 *	24.4	6.5	43	2.7	2.7	nv	1	0.7	0.4	43	1.8
6.12 *	30.4	23.4	-83	2.7	2.7	nv	1	1.0	0.9	-83	1.1
6.48 *	43.7	34.3	-48	2.7	2.7	nv	1	1.5	1.3	-48	1.1
7.19 *	38.1	9.9	-19	2.7	2.7	nv	1	1.1	0.6	-19	1.8
7.52 *	33.6	11.0	-28	2.7	2.7	nv	1	1.0	0.6	-28	1.7
7.87 *	38.5	10.5	-46	2.7	2.7	nv	1	1.1	0.6	-46	1.8
9.57 *	12.5	11.5	-60	2.7	2.7	nv	1	0.4	0.4	-60	1.0
9.93 *	32.0	5.7	-53	2.7	2.7	nv	1	0.9	0.4	-53	2.1
10.26 *	30.0	8.7	-79	2.7	2.7	nv	1	0.9	0.5	-79	1.8
10.52 *	43.7	3.2	-50	2.7	2.7	nv	1	1.2	0.5	-50	2.5

TABLE 3: Stress Data From Site IMS

Depth	Max Horiz Displ	Min Horiz Displ	Azimuth of Max Displ	Max Modulus	Min Modulus	Azim of Max Modulus	Ratio	Max Horiz Stress [Plane Stress]	Min Horiz Stress	Azim of Max Stress	Ratio
m	um	um	E of N	GPa	GPa	E of N	E <sub>max</sub> /E <sub>min</sub>	MPa	MPa	E of N	P/Q
0.79	4.42	0.59	-59	10.2	8.7	-45	1.17	0.5	0.2	-58	2.5
1.07 *	3.37	2.47	25	20.4	15.3	14	1.33	0.8	0.6	20	1.3
1.68 *	4.98	0.53	24	20.4	15.3	14	1.33	1.0	0.4	21	2.6
1.93 *	8.66	-1.42	34	20.4	15.3	14	1.33	1.5	0.3	32	4.7
2.69 *	4.69	-2.80	37	20.4	15.3	14	1.33	0.7	-0.2	37	na
4.50	4.22	-5.86	79	12.4	7.7	14	1.61	0.2	-0.5	81	na
5.26	9.32	0.49	63	10.2	6.5	21	1.58	0.8	0.3	59	2.9
14.63	12.83	3.75	-12	24.6	18.4	19	1.34	3.2	1.6	-6	2.0
20.47	11.14	-0.22	-20	24.5	22.3	22	1.10	2.6	0.8	-18	3.3
21.56	6.15	-0.10	-23	28.6	20.6	15	1.39	1.6	0.4	-17	3.5
21.97	7.81	-0.02	-7	32.4	23.0	16	1.41	2.4	0.6	-4	3.7
26.44 *	5.80	-2.69	-31	20.4	15.3	14	1.33	0.9	-0.1	-27	na
26.90 *	4.44	-0.37	-26	20.4	15.3	14	1.33	0.8	0.2	-20	4.3
27.15 *	6.43	1.08	-18	20.4	15.3	14	1.33	1.3	0.5	-11	2.3
28.12 *	15.79	-0.03	-22	20.4	15.3	14	1.33	2.9	0.9	-16	3.3
28.60 *	11.90	5.70	-15	20.4	15.3	14	1.33	2.5	1.6	-6	1.6

TABLE 4: Stress Data From Sites ADB and RBT

Depth	Max Horiz Displ	Min Horiz Displ	Azimuth of Max Displ	Max Modulus	Min Modulus	Azim of Max Modulus	Ratio	Max Horiz Stress [Plane Stress]	Min Horiz Stress	Azim of Max Stress	Ratio
m	um	um	E of N	GPa	GPa	E of N	E <sub>max</sub> /E <sub>min</sub>	MPa	MPa	E of N	P/Q
ite ADB (Summer)											
1.04 *	42.42	3.07	80	47	47	nv	1	20.0	7.9	80	2.5
1.35 *	9.70	-3.00	14	47	47	nv	1	4.1	0.1	14	41.0
2.39 *	1.61	0.93	41	47	47	nv	1	0.9	0.7	41	1.3
3.94 *	6.64	2.21	72	47	47	nv	1	3.4	2.0	72	1.7
ite RBT (Winter)											
3.35 *	0.65	-0.80	30	47	47	nv	1	0.2	-0.3	30	na
3.87 *	3.90	0.11	-3	47	47	nv	1	1.8	0.6	-3	3.0
4.44 *	0.52	-0.77	40	47	47	nv	1	0.1	-0.3	40	na
4.80 *	0.40	-0.89	50	47	47	nv	1	0.0	-0.4	50	na
5.08 *	0.66	0.27	0	47	47	nv	1	0.4	0.2	0	1.6
6.04 *	0.19	-1.10	38	47	47	nv	1	-0.1	-0.5	38	na
7.90 *	0.80	-0.40	-80	47	47	nv	1	0.3	-0.1	-80	na
8.18 *	3.70	-0.18	62	47	47	nv	1	1.7	-0.5	62	na

### Data Uncertainty

Estimates of measurement error were propagated through calculations in order to estimate resolution of the various parameters in Tables 1 through 4. Uncertainties in the magnitudes of  $U_i$  obtained from borehole deformation curves are relative. At site LRS, large strains allow for reliable values of  $U_i$  to plus or minus 2%. At site IMS, much smaller strains and noisy data result in a plus or minus 10% uncertainty in  $U_i$ . Moduli are determined under relatively controlled laboratory conditions; these deformations can be recorded with plus or minus 0.7% precision, while pressures were recorded with plus or minus 1.0% precision. Errors in the core diameters  $d$  and  $D$  are due to bit wander and wear; it is estimated that these are plus or minus 1.3 mm and 2.5 mm, respectively. The principles of error propagation (Mellor, 1959) allow us to calculate the uncertainty in both rock moduli and stress magnitudes that arise from errors in the parameters used to measure them. For the sum of two numbers  $C = A + B$ , the probable error in  $C$  is given by,

$$c = \pm (a^2 + b^2)^{1/2} \quad (19)$$

where  $a$ ,  $b$  and  $c$  are the uncertainties in  $A$ ,  $B$  and  $C$ , respectively. For a product  $C = AxB$ , and a quotient  $D = A/B$ , the respective errors are:

$$c = \pm (Ax/B) ((a/A)^2 + (b/B)^2)^{1/2} \quad (20)$$

$$d = \pm (A/B) ((a/A)^2 + (b/B)^2)^{1/2} \quad (21)$$

Using equations 19 through 21, and equation 1, the uncertainties in rock moduli are plus or minus 5%, and uncertainties in stresses are estimated at plus or minus 7% for measurements made at LRS, and 12% for site IMS. Errors in stresses measured at site TKY are probably equivalent to those at LRS. Uncertainties for stresses measured at ADB and RBT are greater than those measured at site IMS, due to noisier strain relief curves obtained there. These are estimated at 25%.

To some extent the uncertainty in the orientation of an ellipse depends on the relative magnitudes of its principal axes. Ratios of maximum to minimum axes are thus a measure of this uncertainty. The smaller this ratio becomes, the more circular the ellipse, and the greater the effect of random measurement error on its orientation. Sbar et al. (1984) suggest that a ratio of 1.4 has proven to be a lower limit for reliability in the azimuth of P. For modulus data, this lower limit ratio appears to be 1.05, based on estimates of the error in determining a magnitude for E. Perhaps the greatest uncertainty in orientations of both P and E arise from our inability to accurately measure the orientation of the gauge as it is

situated in the borehole. This uncertainty is estimated to be  $\pm 5^\circ$ .

## Moduli

### Sites LRS and TKY

Twenty-one cores were recovered for moduli measurements at site LRS. Magnitudes of  $\langle E \rangle$ , and orientations of  $E_{\max}$ , are plotted versus depth in Figure 7, while Figure 8 is a rose diagram of the axes of  $E_{\max}$ . Magnitudes of  $\langle E \rangle$  were found to vary by as much as a factor of 3.8 over the entire core, with a mean of 4.18 GPa and a standard deviation of 1.77 GPa. The circular mean orientation of  $E_{\max}$  is N  $85^\circ$  W with a standard deviation of  $18^\circ$ . There is no obvious relationship between modulus orientation and depth in this data set. Magnitudes do, however, appear to be slightly larger in a zone between 7 and 12 m than at other depths.

Examination of Table 1 shows that modulus anisotropy does not have a large effect on data reduction. Typically there is very little difference between the directions of maximum deformation and maximum compressive stress. The correction for modulus anisotropy at LRS rotates axes of inferred maximum horizontal stresses on average less than  $\pm 8^\circ$  from the axes of maximum deformation. There is no consistent pattern to these rotations, illustrating the heterogeneity of this rock

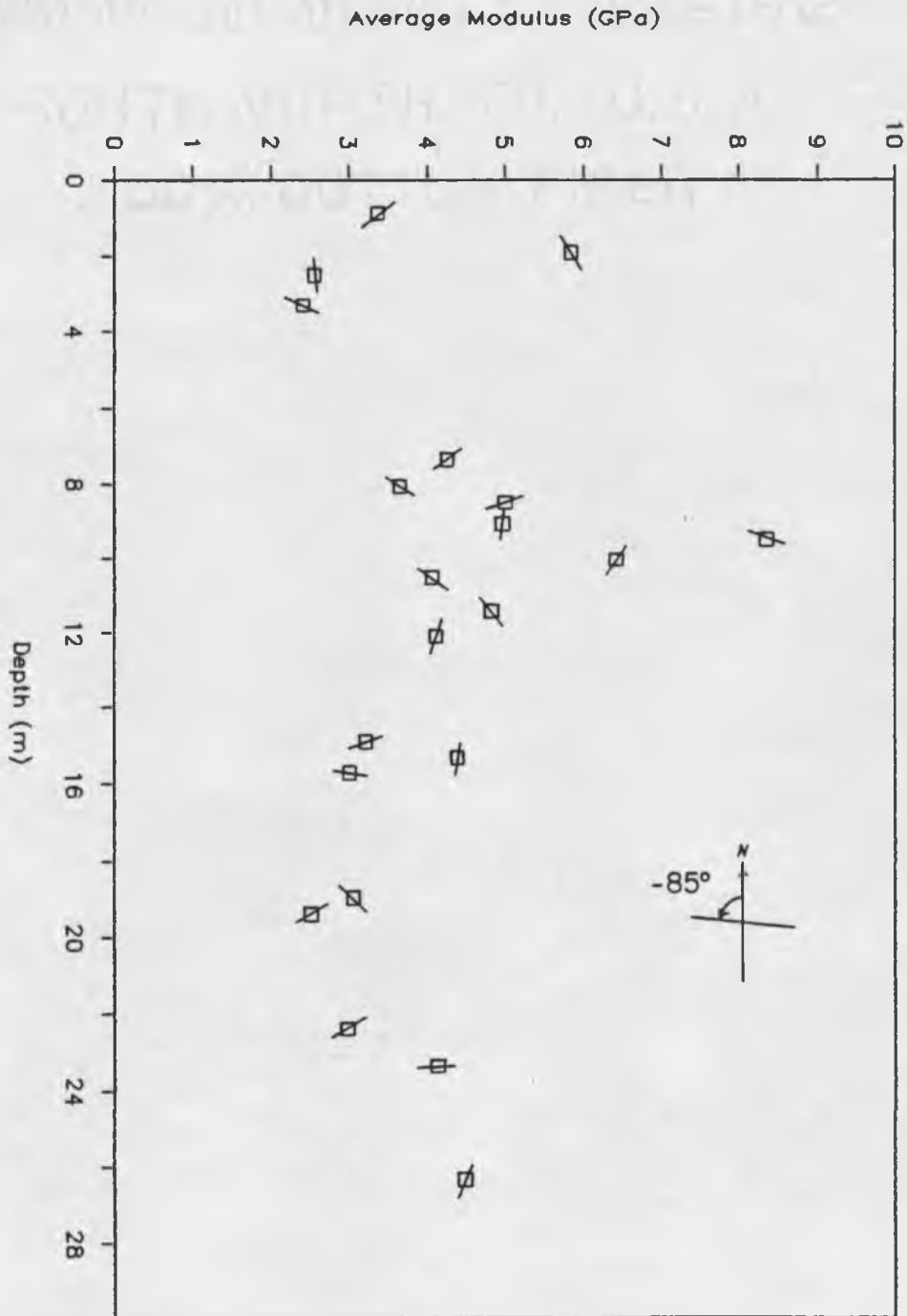


Figure 7. Young's moduli versus depth at site LRS. Squares indicate the magnitudes of average horizontal moduli at each site where a determination was possible. The lines across each symbol indicate the strikes of each maximum horizontal modulus. North is oriented upward, parallel to the depth axis.

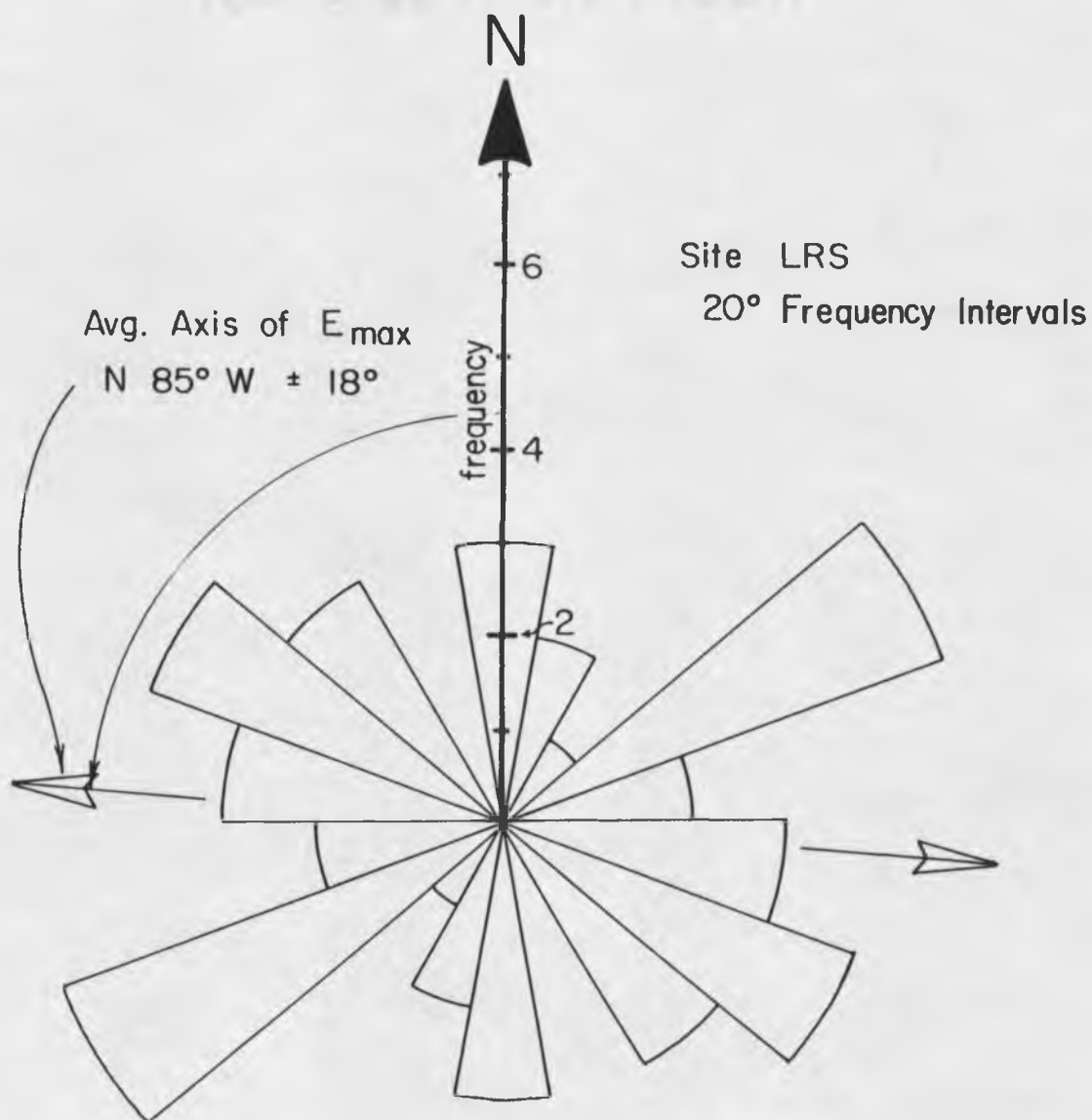


Figure 8. Frequency distribution for axes of maximum Young's moduli at site LRS. The axes of all 21 measurements of maximum moduli at this site are plotted in frequency intervals of  $20^\circ$ . The radial scale is number of observations within each interval.

type. The mean orientation of maximum deformation at LRS is  $N 41^{\circ} W \pm 14^{\circ}$  for all measurements with corresponding biaxial chamber data, while the mean orientation of maximum horizontal compressive stress for these data is  $N 43^{\circ} W \pm 11^{\circ}$ . Thus it can be seen that a net effect of this correction for modulus anisotropy is to slightly reduce the scatter observed in orientations of horizontal maximum stress.

One interesting aspect of the modulus data at LRS is evident in Figure 8, which indicates a bi-modal distribution for the direction of  $E_{\max}$ . One mode is oriented  $N 50 - 60^{\circ} E$ , which is roughly perpendicular to bedding, measured to strike  $N 50^{\circ} W$  with dips of  $50^{\circ} SW$  at the surface. The other mode, more pronounced than the first, is oriented  $N 70^{\circ} W$  which is parallel to the strike of local structure. Reik and Curry (1974) report interesting, and perhaps applicable, results of uniaxial compression tests on Cardium sandstone from Alberta, Canada. They found axes of maximum modulus to be perpendicular to bedding planes, presumably related to sedimentary processes. They also found that moduli measured within bedding planes were anisotropic, with axes of maximum stiffness parallel to local structural trend. Their microscopic analysis of these rock samples revealed a rock fabric in which preferred orientations of microfractures were also parallel to the structural trend.

It is unclear from the data, however, that either bedding orientation or structural trend dominates orientation of maximum modulus at site LRS. The scatter in this data set may reflect uncertainties in measuring the moduli. Other factors at site LRS include cross bedding and the heterogeneous composition of the rock. This illustrates the importance of orienting the gauge at the same location during both strain measurement and biaxial testing. It also illustrates why an average isotropic modulus should be used to reduce measurements which lack biaxial chamber data at this site. Modulus data is simply too variable in this sandstone to accurately predict anisotropic behavior between measurements. For these reasons, an average isotropic modulus of 4.18 GPa was used to calculate stresses for measurements without biaxial chamber data at site LRS.

In an attempt to increase the size of the data set for tectonic interpretation, measurements made during a previous field season at site TKY have been re-interpreted. The results are presented in Table 2 and Figures 12 and 15. An average isotropic modulus of 2.7 GPa was used to calculate stresses from borehole deformation. No attempt was made to correct these data for anisotropy.

There are two important differences between measurement techniques for moduli at sites TKY and LRS. First, biaxial chamber data at TKY were taken while loading

each core sample to a maximum pressure of 1.45 MPa. No unloading data is available at site TKY. Second, moduli at TKY were measured in the field, within days of removal of the core from the ground. This is in contrast to those of LRS, where biaxial chamber tests were not made on core until the end of the field season, up to two months after it was taken from the ground. The effects of loading versus unloading moduli determinations can be seen in Figure 3. The unloading portion of the cycle for component one of the sandstone yields a modulus which is considerably larger than that of the loading portion. Results were similar on most of the sandstone core sampled at LRS. The average increase between unloading and loading moduli was a factor of 1.4.

The effects of aging on core samples taken from LRS, unfortunately, were not measured. Tullis (1981), however, reports the effects of aging on a sample of sandstone core taken from a nearby site using the same technique. In only a few days time, the core's average modulus was found to increase by a factor of 1.4 over the value it had when tested immediately upon removal. Although this is suggestive of a systematic effect of aging, no correction was applied to the data at LRS because of a lack of supporting evidence.

Thus the isotropic modulus reported in Table 2 is an average computed from loading deformations measured on

all core sampled at TKY, multiplied by a factor of 1.4 only to account for differences between loading and unloading secant moduli at this site.

#### Site IMS

Seven oriented core segments were retrieved for modulus determinations at site IMS. At depths of 1-3 m, and 26-29 m, the core was so highly fractured that it was impossible to measure moduli with the biaxial chamber. Successful modulus measurements are plotted with depth in Figure 9. Figure 10 shows a rose diagram of the orientations of all seven axes of maximum E.

Two points are illustrated by Figures 9 and 10. First, moduli increase in magnitude with depth at this site, from an average of 8 GPa near the surface to approximately 26 GPa at 22 m. Average values of E have approximately the same scatter between adjacent measurements as found at site LRS. Second, with the exception of a single NW measurement at 0.79 m depth, the orientations of  $E_{\max}$  were found to tightly cluster about a NNE direction. Below this anomalous measurement at 0.79 m, no change in orientation of  $E_{\max}$  was recognized with depth.

Azimuthal consistency at this site allowed the use of an anisotropic average modulus to reduce stress data which lacked biaxial chamber information. Average values for  $E_{\max}$  and  $E_{\min}$  were found to be 20.4 GPa and 15.3 GPa,

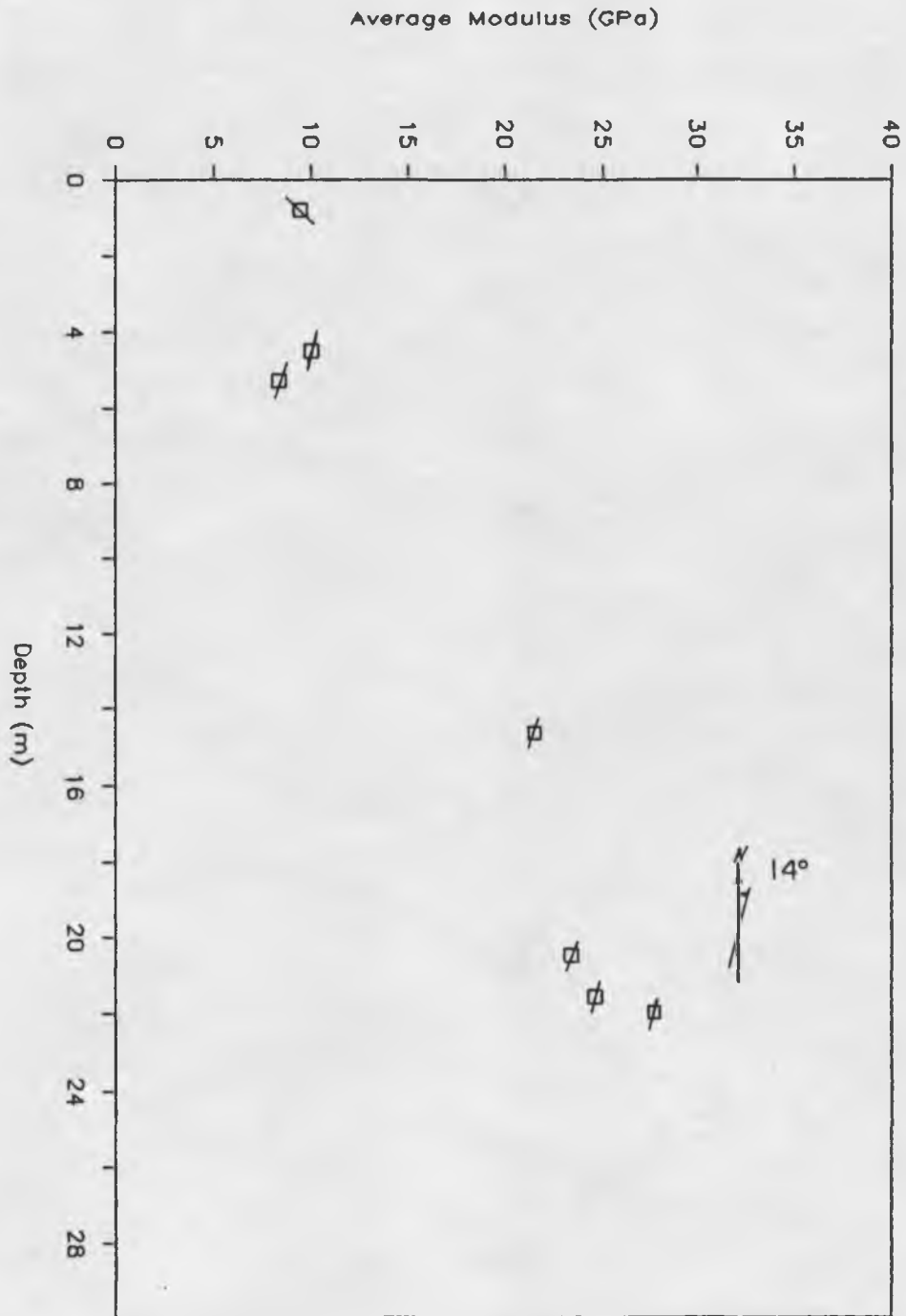


Figure 9. Young's moduli versus depth at site IMS. For other details, see Figure 7.

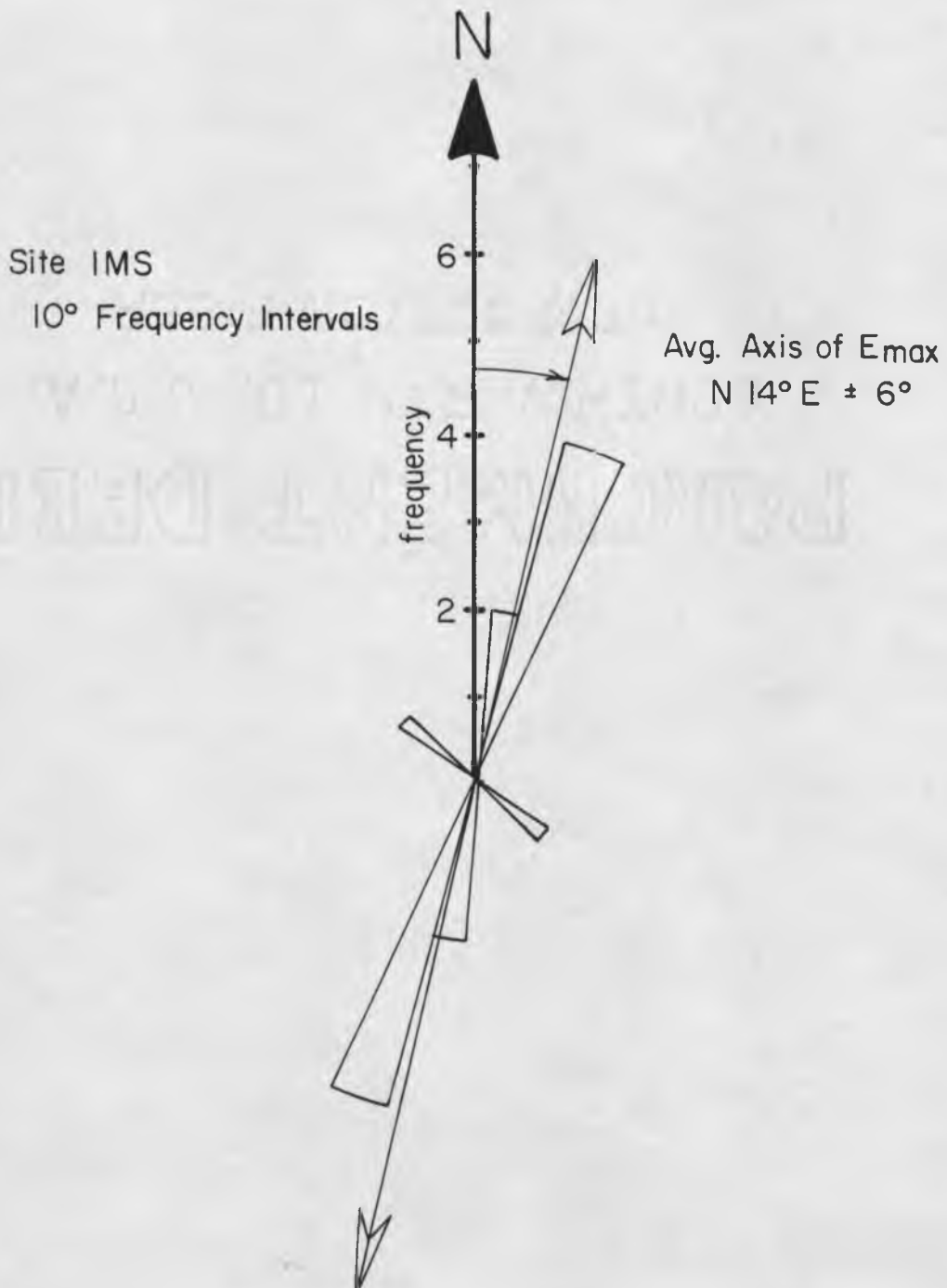


Figure 10. Frequency distribution for axes of maximum Young's moduli at site IMS. A total of seven modulus measurements were made at this site. Radial scale is number of observations within 10° frequency intervals.

with standard deviations of 9.3 and 7.4 GPa, respectively. The circular mean orientation of  $E_{\max}$  was found to be N 14° E with a standard deviation of 6°.

A first order correction for modulus anisotropy had a more consistent effect on the inferred orientations of P axes at this site than at LRS, mainly because of the strongly anisotropic nature of the rock at IMS. On average, axes of maximum deformation were rotated 4° clockwise from the corresponding axes of maximum displacement at IMS. This is in contrast to + 6° observed at LRS.

#### Sites ADB and RBT

As with site TKY, sites ADB and RBT represent re-interpretations of data from previous field seasons. Biaxial chamber data at these sites were also only recorded during a loading cycle. Inspection of Figure 3 shows that hysteresis is negligible in the quartz monzonite at site IMS. The difference in secant moduli between loading and unloading portions of the curve is therefore insignificant. It is assumed that the granite at sites ADB and RBT would have similar characteristics to the quartz monzonite at IMS. There is significantly more scatter in orientations of  $E_{\max}$  measured at these sites than was measured at site IMS, however. For these reasons, an average isotropic modulus was calculated for this site, and used to calculate stresses. This was found to be 47.2 GPa, with a standard

deviation of 11.4 GPa. It was not adjusted for nonlinearity or hysteresis.

## CHAPTER 4

## RESULTS

Thermal StressesSites LRS and TKY

Results at site LRS, presented in Table 1, are striking in two features. First, the magnitudes of both maximum and minimum plane stress decay from 4.3 MPa near the surface, to about 1.3 MPa at a depth of 10 m. Below this depth the magnitudes slowly increase with depth. Second, the orientations obtained for P show significant scatter near the surface, where the ratios of P/Q are small; those measured below 6 m have a ratio P/Q generally greater than 1.4 and have a more consistent NW orientation. Data from site TKY are similar, except that the maximum depth sampled was 11 m. Near surface behavior at both sites strongly suggests a thermal origin for stresses due to seasonal surface temperature variations. To investigate this hypothesis, monthly average temperatures were computed from data collected at nearby Palmdale airport (NOAA, 1978; 1979; 1980), and are shown in Figure 11 for the period 1978-1980. Superimposed on this data is the best sinusoidal fit for the two years immediately preceding the 1980 summer field season. The average monthly ambient temperature at Palmdale was found to oscillate about a mean annual temperature of 16°C, with a period of 1 year and amplitude

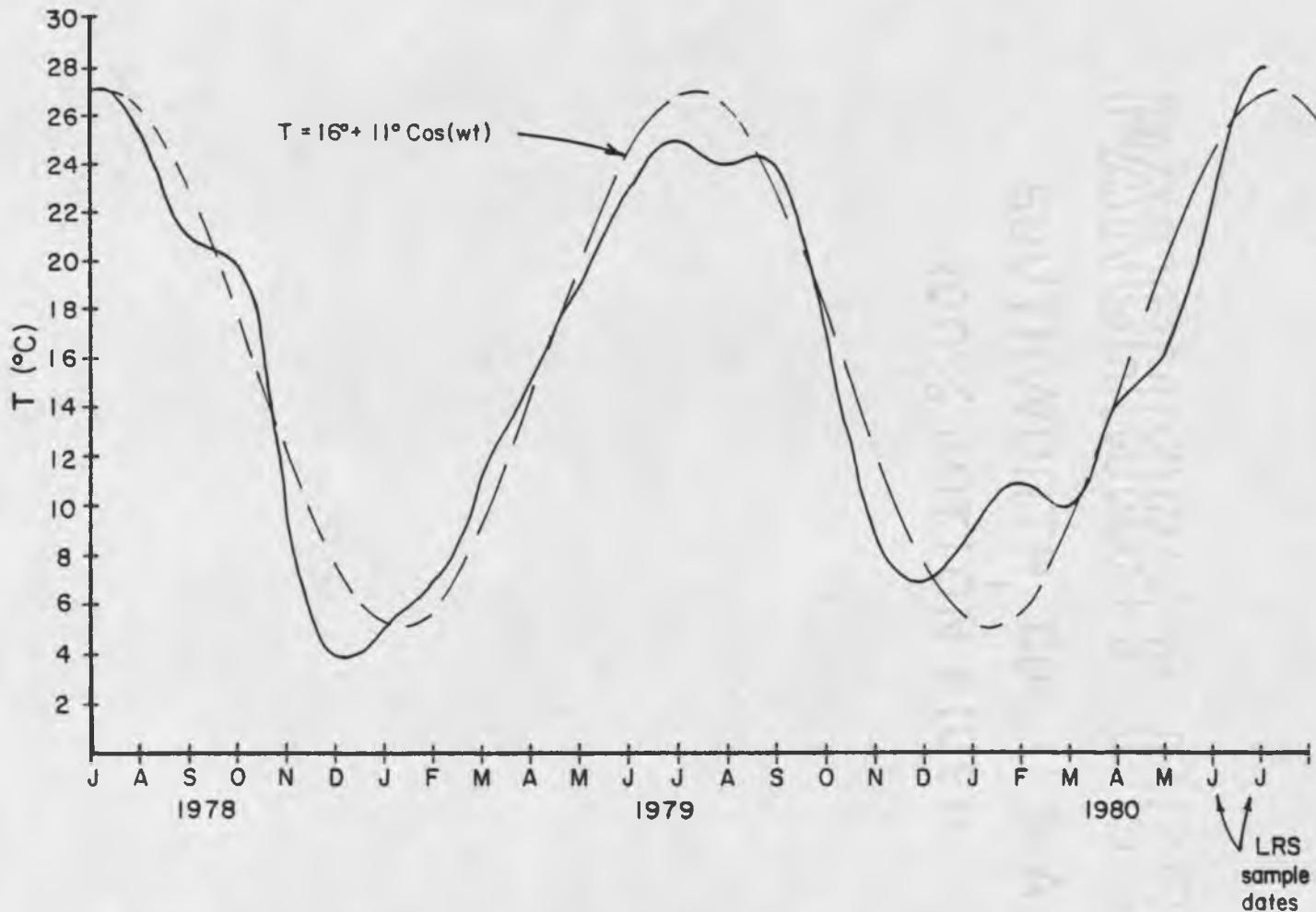


Figure 11. Monthly average surface temperatures for the Palmdale, California airport. Temperature data is represented by the solid curve. The dashed curve is the best fitting sine function used to calculate a temperature distribution in local rock outcrops. Site LRS was sampled during the end of June, 1980.

= 11°C. The cosine function was adjusted to coincide with peak temperature observed during the month of July. Time  $t=0$  corresponds to the peak temperature in July of 1978, and the arbitrary phase angle is set to zero.

Based on observations at Palmdale airport, one can model the temperature profile expected in local outcrops using equation 18. Sampling at LRS commenced June 16th 1980, while sampling at TKY commenced June 29th 1979, both of which are less than a month prior to the peak temperature excursion of 11°C. Values of  $t=6.0530 \times 10^7$  sec,  $k=1.4 \times 10^{-6}$  m<sup>2</sup>/s,  $v=0.4$ , and  $\langle E \rangle = 4.18$  GPa are assumed for the outcrop. The thermal stress profile from equation 15 matches the average stress magnitudes found at both sites LRS and TKY, provided  $\alpha = 3.5 \times 10^{-5}$  /°C and a background stress of 1.3 MPa exists at this site. Average stress magnitudes, as well as orientations of maximum horizontal compressive stress at both TKY and LRS, are plotted in Figure 12, with the modeled thermal and background stress profile superimposed.

It is evident from Figure 12 that seasonal thermal variations have a negligible effect on stress magnitudes below 14 m depth. The mean stress computed from the data below this depth at LRS is  $1.3 \pm 0.6$  MPa, justifying its use as the background stress at this site. A coefficient of thermal expansion equal to  $3.5 \times 10^{-5}$  /°C is a factor of 2.7 larger than the maximum found tabulated for sandstone,

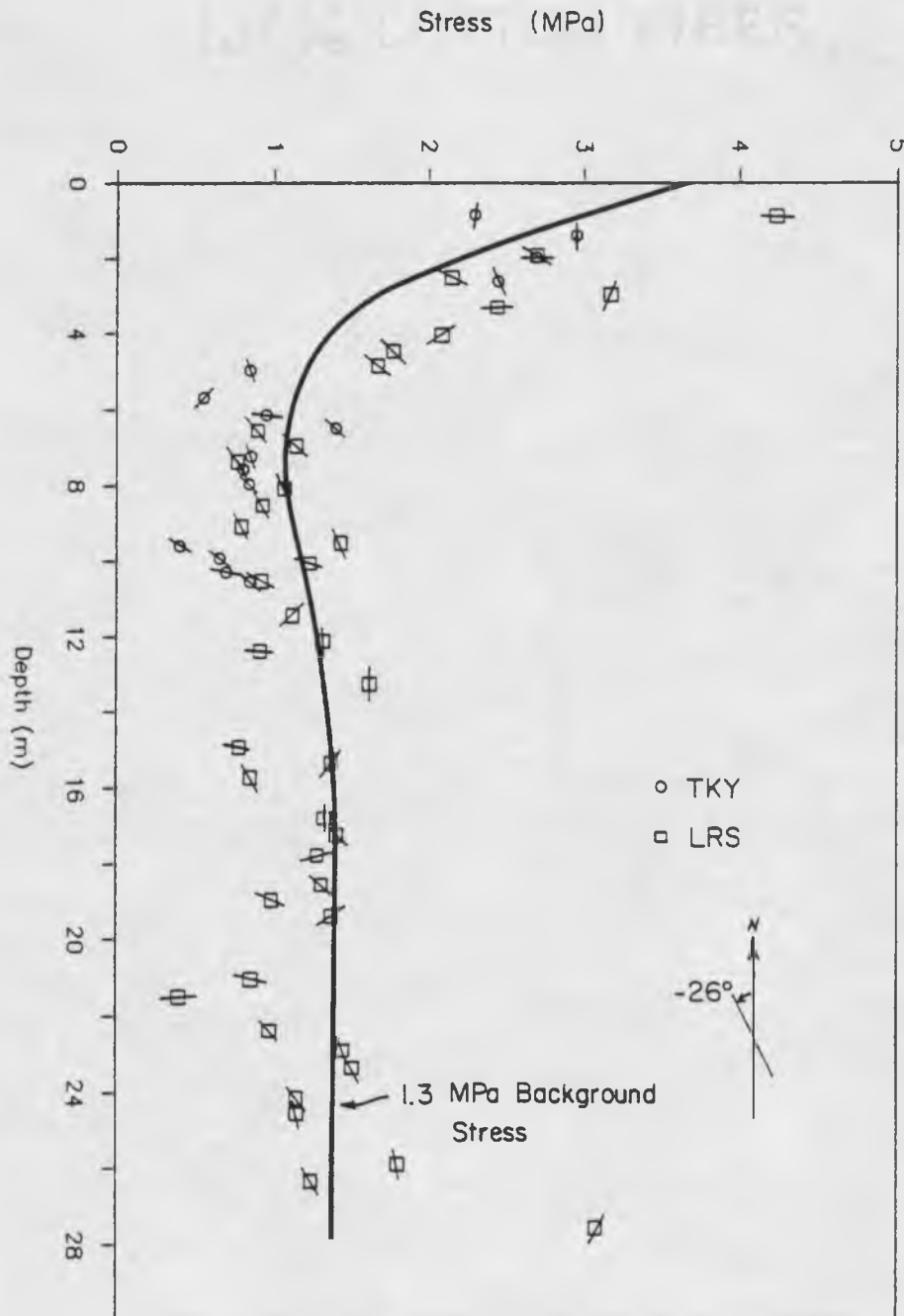


Figure 12. Horizontal stresses versus depth at sites LRS and TKY. Squares and circles are the average horizontal stresses at LRS and TKY, respectively. The line at each symbol is the orientation of each axis of maximum compressive stress,  $P$ . North is oriented upward, parallel to the depth axis. The solid curve is the best fitting thermal stress profile predicted by equation 15, decaying to a 1.3 MPa background stress below 16 m.

however (Roy, et al., 1981; Clark, 1966). There are at least three possible explanations for this discrepancy. First, the coefficient of expansion for this rock may indeed be high. Second, seasonal heating of this outcrop may be greater than ambient temperatures at Palmdale reflect. Third, the modulus determined in biaxial chamber tests, while applicable to the stress relief process, is not appropriate for stresses generated by thermal expansion. None of these can be verified with the existing data. It would have been instructive to measure the temperature distribution and thermal properties of this rock in situ, thereby minimizing their respective uncertainties. The third explanation does seem the most significant however, considering the non-linear nature of the modulus for this rock (Figure 3). This outcrop may be stiffer, when loaded with a background stress of 1.3 MPa, than a secant modulus predicts. It may also be incorrect to assume that a secant modulus is appropriate to an incremental process such as is experienced during thermal expansion. Ultimately, a factor of two or three is considered acceptable, in light of the factor of three variability in modulus magnitudes measured at this site.

Stress orientations, as well as magnitudes, reflect thermal effects at site LRS. Figure 12 also shows the scatter in orientations of P observed at shallow depths where magnitudes are abnormally high. This scatter becomes

minimal by 6 m depth, where thermal stresses are a small fraction of the background stress. All six orientations above 4.4 m depth at LRS are poorly resolved, as evidenced by their ratios of maximum to minimum stress of less than 1.4. Figure 13 is a rose diagram of the orientations of P, for those measurements in which the ratio of  $P/Q \geq 1.4$ , and depth greater than 6 m. The circular mean and standard deviation determined for this data set are  $N 26^{\circ} W \pm 11^{\circ}$ . At shallow depths, isotropic thermal stresses simply overwhelm any anisotropic background stress field that might exist in this outcrop. Other zones show scatter in orientations of P, notably at 17-19 m and 22-25 m depth, which is further evidence of the heterogeneous nature of this rock.

A thermal stress field within the uppermost 6 m of an outcrop is isotropic, provided the rock is homogeneous and perfectly constrained. Modulus anisotropy is one possible source for an anisotropic thermal stress field, however. In Figure 14, the orientations of P shallower than 6 m are plotted in a rose diagram. When compared with Figure 8, a similarity can be seen between the average orientation of P,  $N 72^{\circ} W$ , and one of the two lobes of maximum stiffness observed in core samples at LRS, also approximately  $N 70^{\circ} W$ . The argument can be made that thermal stresses build up along one of the two common axes of maximum modulus in this outcrop. The argument is far

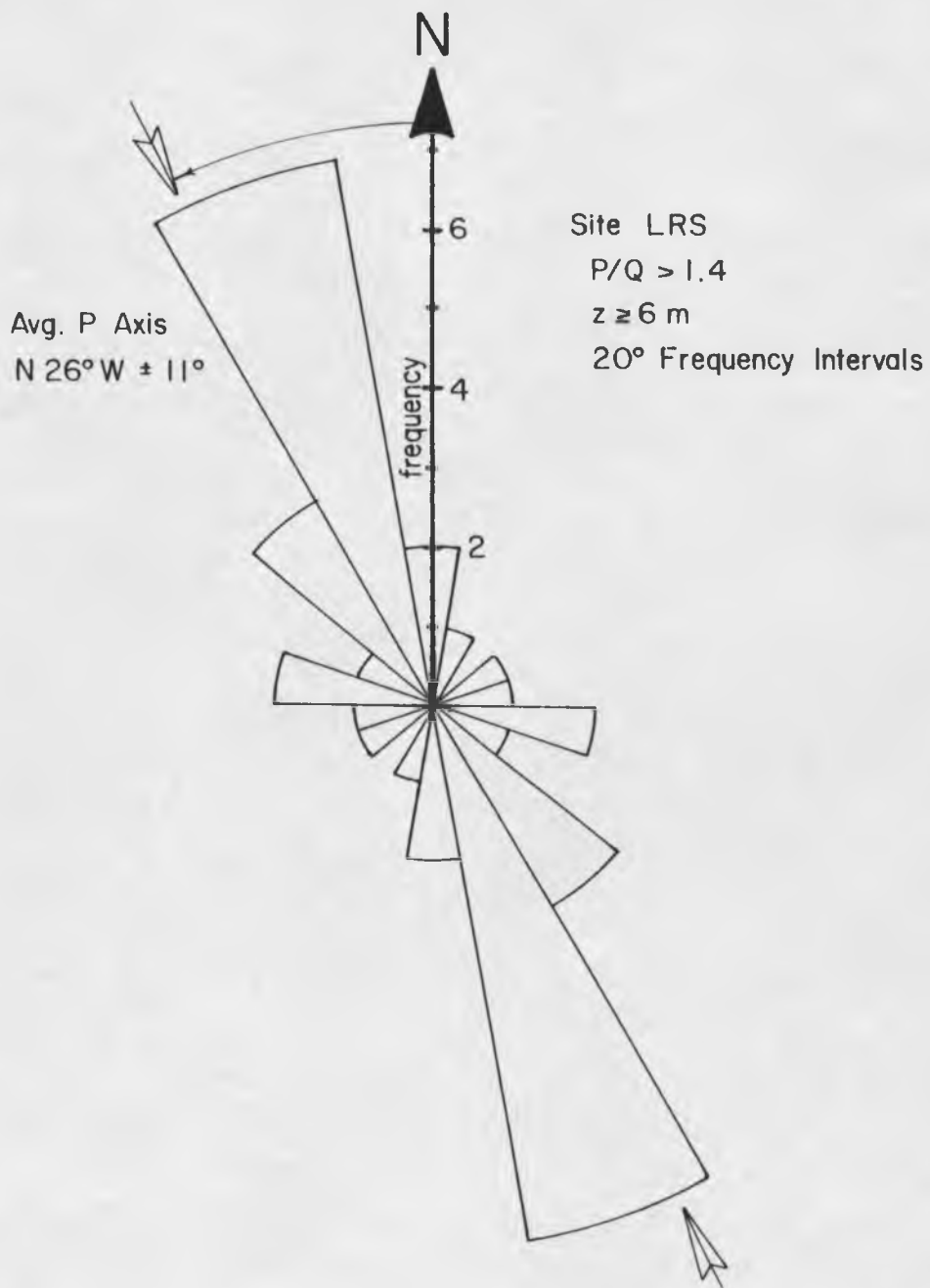


Figure 13. Frequency distribution for P axes at site LRS with ratio of maximum to minimum horizontal compressive stress,  $P/Q$ ,  $\geq 1.4$ , and depth  $\geq 6$  m. For other details, see Figure 8.

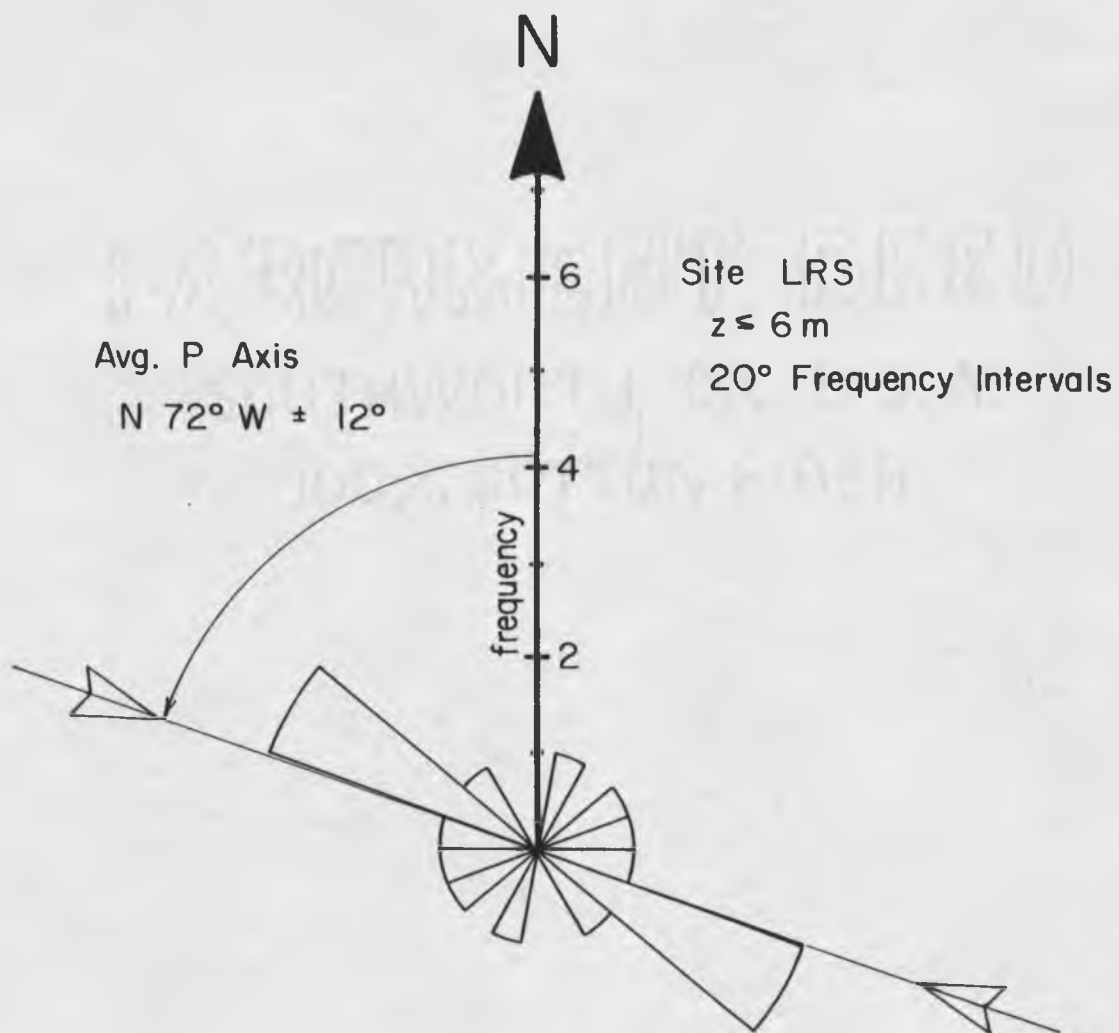


Figure 14. Frequency distribution for P axes at site LRS at depth  $\leq 6$  m.

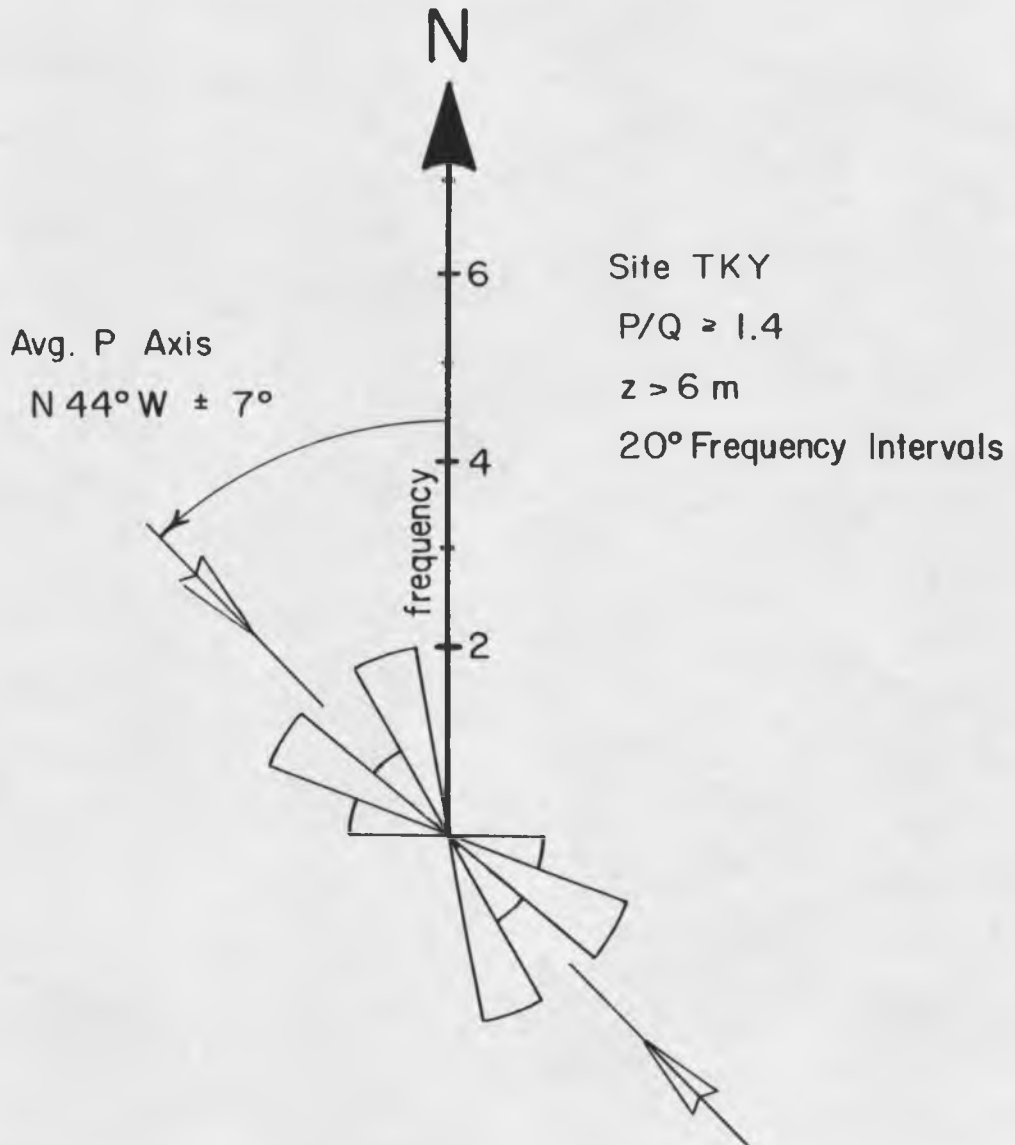


Figure 15. Frequency distribution for P axes at site TKY with ratios  $P/Q \geq 1.4$  and depth > 6 m.

from conclusive, however, with such a small sample size of measurements made within 6 m of the surface.

Stress orientations measured at site TKY show more scatter than at site LRS, principally because few measurements were made deeper than 6 m. The mean orientation of those data at TKY with ratios of  $P/Q \geq 1.4$ , at depths greater than 6 m, is N  $44^{\circ}$  W, with standard deviation of  $7^{\circ}$ . These data are illustrated in a rose diagram in Figure 15.

#### Site IMS

Results at site IMS are illustrated in Figure 16, where the orientations of P axes, and the average horizontal stress magnitudes, are plotted with depth. At this site, no exponential decay in stress magnitudes is observed with depth. In fact, surface stresses are quite low, averaging less than 1.0 MPa. Surface stresses do, however, exhibit markedly different orientations than were found at depth. Within 6 m of the surface, with one exception, P is found to be oriented NE. At greater depth, P is consistently found to be NNW in orientation. The expected thermal stress profile for this rock type is shown as the solid curve in this figure, assuming values of  $k=1.3 \times 10^{-6} \text{ m}^2/\text{sec}$ ,  $\nu=0.2$ , and  $\alpha=8 \times 10^{-6}/^{\circ}\text{C}$  (Clark et al., 1966). A Young's modulus of 17.8 GPa and  $t=5.913 \times 10^7$  sec are used for this outcrop, corresponding to  $\langle E \rangle$  measured in

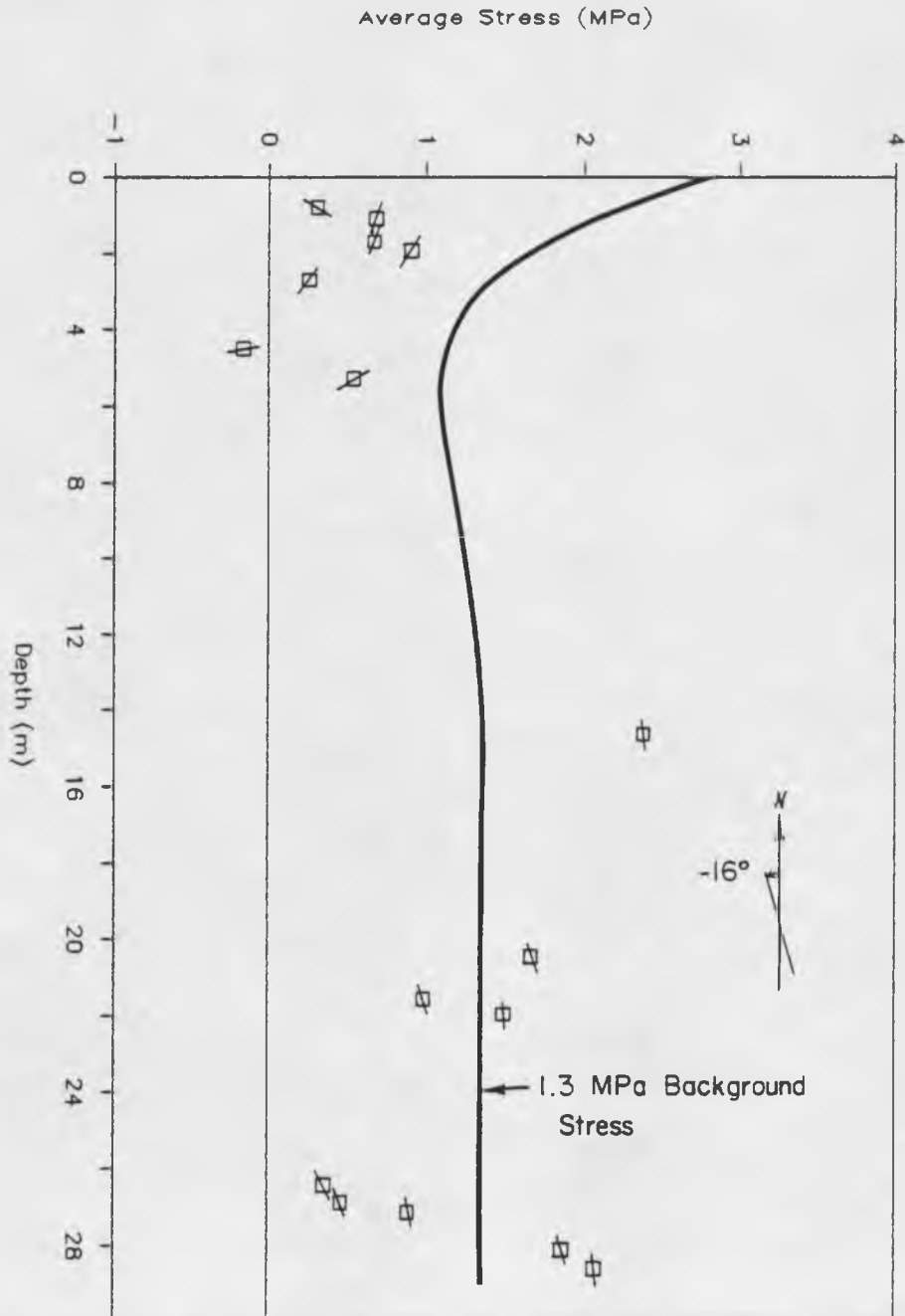


Figure 16. Horizontal stresses versus depth at site IMS. Solid line is the thermal stress predicted for quartz monzonite by equation 15. For other details, see Figure 12.

biaxial tests, and the June 1 start date for sampling at this site. The stress at depth on this thermal profile is adjusted to match the average of 1.3 MPa measured below 6 m at this site. This background stress magnitude is consistent with that measured at depth at site LRS, though there is considerably more scatter in magnitudes at this site.

The apparent lack of thermal stresses in this outcrop can be explained by a highly fractured surface rock. This also explains why stress orientations near the surface are so dissimilar to those at depth. A N 40° E striking fracture set dominates the surface at this borehole. Two separate fractures, dipping 80° to the SE, intersect the borehole within 7 cm of the first three measurements. A third fracture with the same strike was encountered adjacent to the measurement at 1.93 m, and found to turn to vertical dip, exiting the borehole at approximately 4 m depth. All these surface fractures were open, and highly weathered, as evidenced by mineralization on the faces of fragments recovered. Other fractures evident within the borehole had strikes and dips of N 70° W - 45° SW, N 50° W - 65° SW, and N 25° W - 40° NE. These fracture patterns were found in unbroken core segments, indicating they were generally closed and less highly weathered. A detailed joint study was not conducted of this outcrop, however the dominant fracture strike at the surface appeared to be NE in orientation with steep dips,

cut by a lower density of fractures striking WNW with steep dips. The net result is a surface rock which is so highly fractured that significant thermal stresses cannot build up in the surface rock. Below 6 m, fractures were generally closed and less deeply weathered, presumably allowing the transmission of a regional stresses field.

Surface stresses that do exist at site IMS have an average orientation of P of  $N 43^{\circ} E \pm 9^{\circ}$ , for depths less than 6 m, as shown in Figure 17. This is roughly parallel to the dominant fracture orientation in this outcrop. Five out of seven of these measurements were made within one borehole diameter of NE striking, steeply dipping fractures. Thermal expansions are obviously less confined perpendicular to fracture strike, hence less thermal stress can accumulate in this direction. At depths below 6 m, the average direction of maximum horizontal compressive stress is  $N 16^{\circ} W \pm 3^{\circ}$ , as shown in the rose diagram of Figure 18. This orientation is not parallel to any observed fracture pattern, increasing the likelihood that, in fact, tectonic stresses are being measured.

#### Sites ADB and RBT

Stress magnitudes, and the orientations of P axes at sites ADB (summer) and RBT (winter) are plotted with depth in Figure 19. Summertime measurements appear to indicate that thermal stresses can build up at this site.

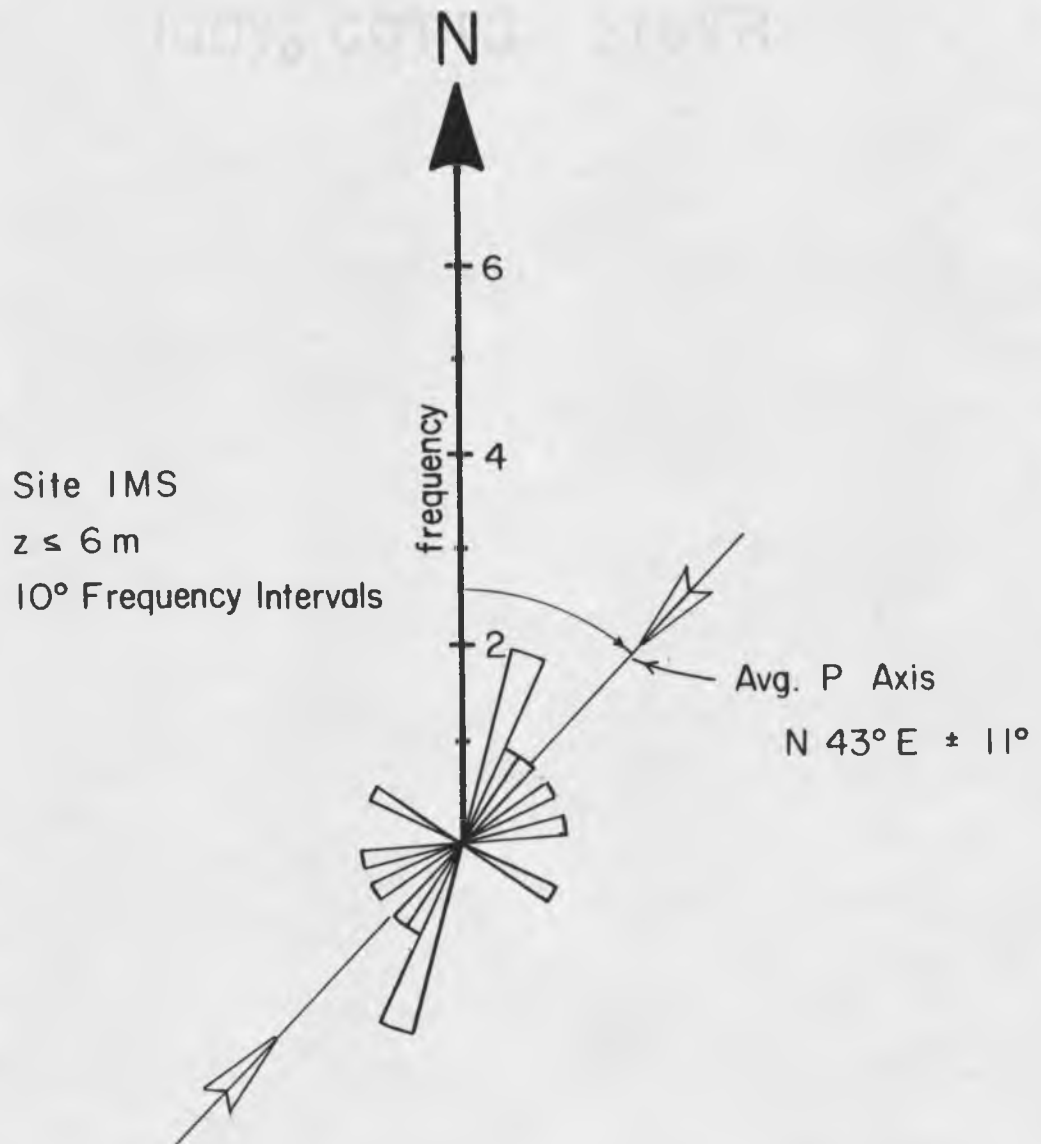


Figure 17. Frequency distribution for P axes at site IMS within 6 m of the surface.

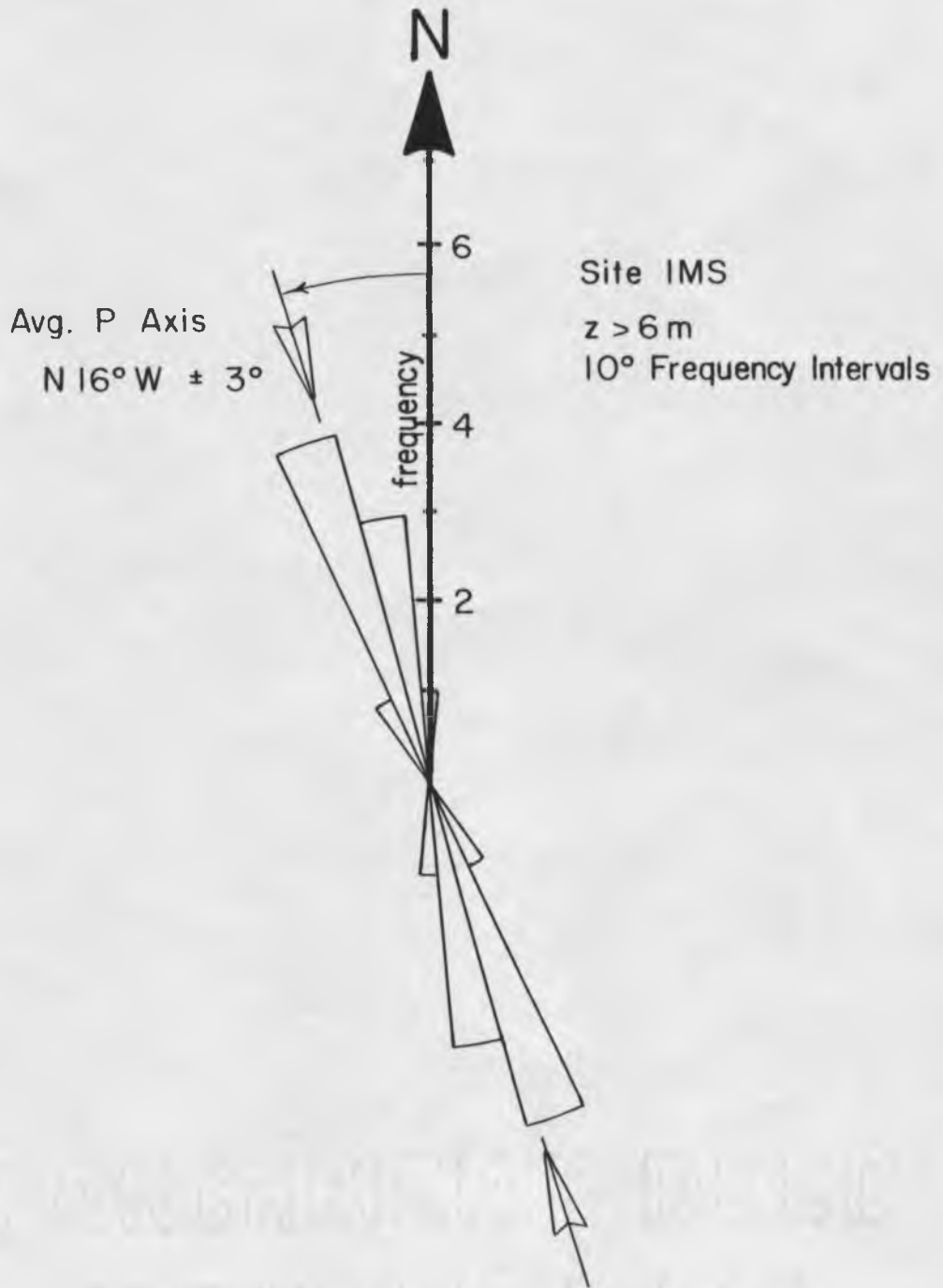


Figure 18. Frequency distribution for P axes at site IMS deeper than 6 m.

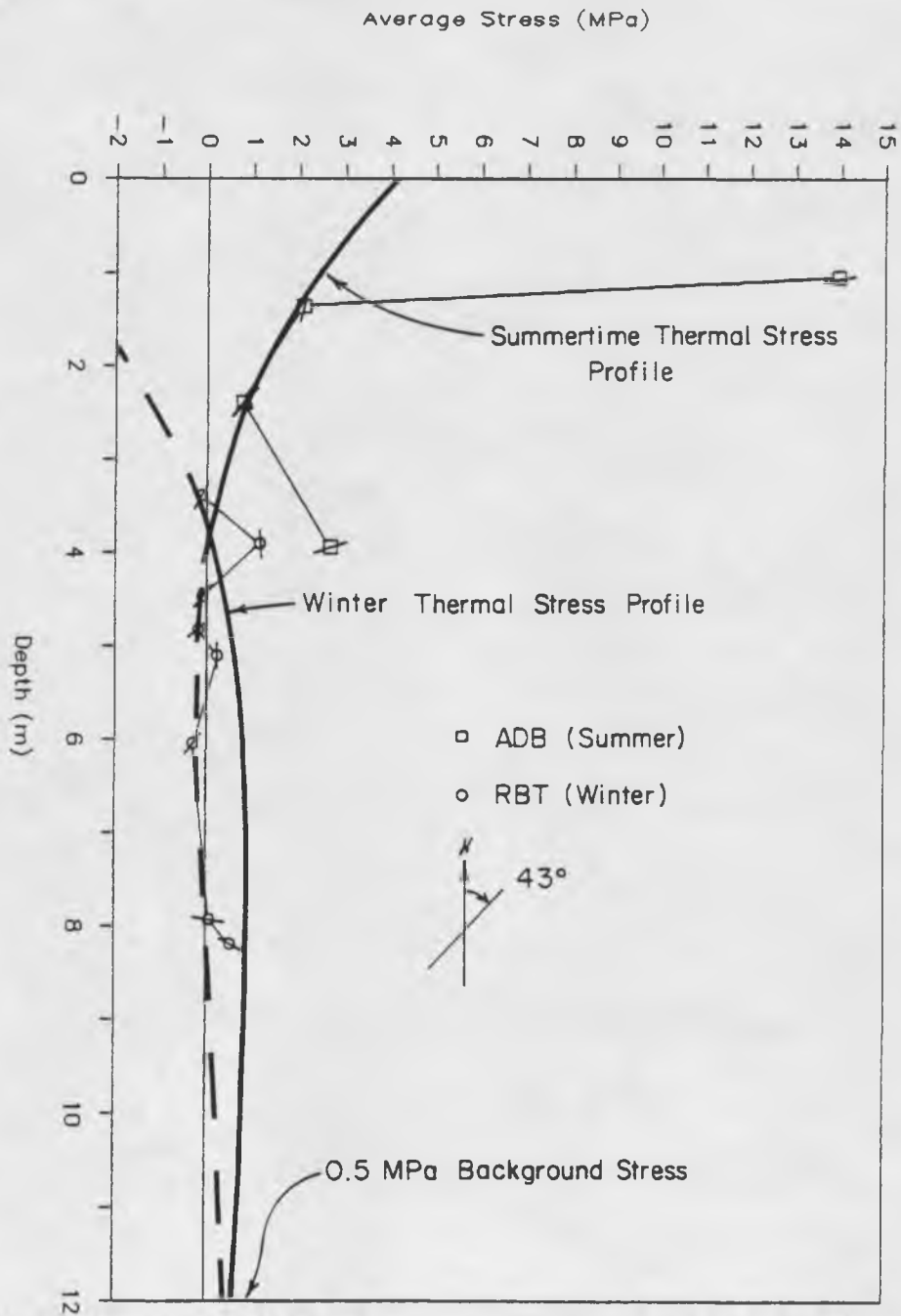


Figure 19. Horizontal stresses versus depth at sites ADB and RBT. Thermal stresses in granite for both summer and winter are superimposed on the data. The solid portion of the summer stress profile refers to summer measurements (squares). The solid portion of the winter stress profile refers to winter measurements (circles). Both stress profiles converge to a 0.5 MPa background stress below 12 m. For other details, see Figure 12.

Using values of  $k$  and  $\alpha$  equal to those at site IMS, and the average modulus of 47 GPa determined for this granite, thermal stress profiles for both summer and winter are also shown in Figure 19. A background stress of 0.5 MPa is assumed at depth.

Taken by themselves, the stress measurements from sites RBT and ADB are not convincing examples of a thermal origin. Summertime measurements number only four, all of which are within 4 m of the surface. Winter measurements were all made at depths greater than 3 m, so that the two data sets unfortunately overlap by only 0.6 m. They do lend support to results from site LRS, however. Winter measurements give essentially zero stress at 3-4 m depth, while summer measurements yield a slightly positive stress at 3 m. It is assumed that significant tensile stresses due to seasonal temperature variations cannot develop in a fractured rock such as is encountered here, hence a zero winter stress is expected near the surface.

#### Tectonic Stress

Maximum horizontal stress orientations measured below 6 m at sites LRS and IMS are mutually consistent, an indication of a possible common source. At site LRS, data with ratios of  $P/Q \geq 1.4$  yield a mean of  $N 26^{\circ} W \pm 11^{\circ}$  for data taken deeper than 6 m. At site IMS, the orientation for maximum horizontal stress below 6 m is  $N 16^{\circ} W \pm 3^{\circ}$ ,

within one standard deviation of the mean at site LRS. At site TKY, agreement with data from LRS and IMS is less convincing. Here, the mean orientation of P for ratios of  $P/Q \geq 1.4$ , and depth greater than 6 m, is  $N 44^{\circ} W \pm 7^{\circ}$ . This  $18^{\circ}$  difference between the mean orientations of P at sites LRS and TKY can be reconciled, given the fact that an isotropic modulus was used at TKY, and the data are from a relatively small sample size ( $n=6$ ). For these reasons azimuthal data from site TKY was considered of poor quality, and therefore not incorporated into an average stress orientation at LRS. At sites ADB and RBT only two measurements were made deeper than 6 m, both during the winter season. These data show too much scatter to make a meaningful interpretation of the orientation of maximum horizontal stress at this site.

Agreement is excellent between the direction of maximum compression determined in this study, and that determined by deep hydrofracture techniques in the immediate vicinity. Zoback et al. (1980) report an average of  $N 20^{\circ} W \pm 15^{\circ}$  for the western Mojave desert, from tests in three wells to depths of 850 m. The locations of these wells relative to sites IMS and LRS are indicated in Figure 6. Agreement is also good with the azimuth of maximum shortening measured over 13 years in the Palmdale area by Savage and Gu (1985). Strains measured on the Palmdale geodetic net imply an axis of maximum horizontal shortening

which is oriented NNW.

Stress orientations determined in this study are also consistent with directions for maximum horizontal stress measured by Tullis (1981), using similar shallow stress relief techniques in the western Mojave desert. Tullis (1981) sampled outcrops in the immediate vicinity of site LRS, and reported orientations of P at three sites to be  $N 44^{\circ} W$ ,  $N 15^{\circ} W$ , and  $N 27^{\circ} W$ , in general agreement with this study. Sbar et al. (1979), on the other hand, sampled the neighboring outcrops with the same technique, and reported  $N 57^{\circ} W$ ,  $N 31^{\circ} E$ , and N-S, which do not agree with this study. The aforementioned studies share two things in common. Measurements were made at shallow depth (less than 2.5 m), and only a few measurements were made at each site. Both factors contribute to the widely varying stress orientations recovered.

The state of stress in the vicinity of the big bend of the San Andreas fault in southern California is at best complicated. If stresses measured during this study are to be interpreted as tectonic in origin, they must compare favorably with those measured by others, particularly with those techniques which sense to greater depth, out of the realm of thermal and topographic effects. Studies of earthquake focal plane solutions over the entire San Andreas fault system suggest that the orientation of far field compressive stress is  $N 14^{\circ} E \pm 9^{\circ}$  (Sbar, 1982).

Near field stresses, as measured by in situ techniques, generally yield a NNW orientation for the maximum horizontal compressive stress in the vicinity of the big bend of the San Andreas fault, approximately  $45^{\circ}$  clockwise from fault strike. The finite element models of Richardson and Bergman (1979), and Sbar and Richardson (1981), show that the two results are compatible if one considers the effect of fault geometry and a compliant fault zone on the regional stress field. In these models of the San Andreas and Garlock fault systems, a NNE far field stress orientation is shown to rotate to NNW in the region of the big bend. The amount of rotation depends upon the relative compliance of the fault zone and the surrounding elements, as well as the fault geometry. The major point illustrated by these models is that the local stress field surrounding a fault is dictated by the fault geometry and its physical properties, and therefore is not easily predicted.

Current work on the stress field surrounding the San Andreas fault in California has concentrated on the interpretation of well bore breakouts within existing petroleum and newly drilled scientific wells (Zoback et al., 1985; 1987; Springer, 1987). In this technique, the walls of a borehole are examined with a televiewer, and/or a conventional four arm dipmeter common to the petroleum industry. Diametrically opposed breakouts result in an elongated cross section of the borehole, aligned with the

axis of minimum principal stress. Thus, a log of the orientations of the maximum horizontal principal stresses can be obtained with depth in almost any existing well (Plumb and Hickman, 1985; Zoback et al., 1985).

Three recent studies of in situ stresses have been conducted near the San Andreas fault, each pertinent to the investigation of near field stresses associated with an active fault. In one, Springer (1987) determined borehole elongations from four arm dipmeter logs of 10 petroleum wells in the Coalinga area, located approximately 200 km to the north of Palmdale. The axes of maximum horizontal compressive stress were found to be oriented NE, perpendicular to the major fold axes in the San Joaquin valley, and at a 70 to 90° angle to the major strike slip faults in the region. In a second study, both hydrofracture and borehole elongation studies have been conducted to a depth of about 2 km in the Cajon Pass research well, located 40 km to the SE of the Palmdale area, and (Springer et al., 1987; Zoback et al., 1987). In this well, the axis of maximum compression was found to be oriented N 70° E, approximately 125° clockwise from the local strike of the San Andreas fault. In a third study, hydrofracture techniques on the Black Butte well, located 20 km NE of site LRS, yield a N 40° E orientation for the maximum compressive stress. This orientation is 105° clockwise from the local strike of the San Andreas fault, and 60° clockwise from the orientation

inferred at site LRS and IMS (Stock et al., 1986).

Springer's (1987) study in the Coalinga area reveals a San Andreas fault zone in central California that has so little strength that it can support little or no shear stress. The result is a near fault stress field that is rotated  $35^{\circ}$  clockwise from the far field orientation, nearly perpendicular to the fault which strikes approximately  $N 20^{\circ} W$  in this region. Fault rheology in southern California is clearly different than the region to the north, however, as evidenced by the NNW orientations for maximum compressive stress obtained by in situ stress measurements. While data in this region is not as abundant as in central California, it implies that the San Andreas fault in the region of the big bend can support significant shear stress. This results in a counter-clockwise rotation of the maximum compressive stress, to a NNW near field orientation.

Both the Black Butte and Cajon Pass wells yield stress orientations and magnitudes which seem incompatible with the model of a San Andreas fault with shear strength in the Palmdale region. Results from both wells indicate a lack of significant shear stress on planes parallel to the fault at depths of about 2 km, and axes of maximum compression are oriented ENE (Zoback et al., 1987). These isolated examples appear to reflect local heterogeneities, however. Cajon Pass well is located within 2 km of the

Cleghorn fault, where recent left lateral and normal slip contrasts with the right lateral sense of motion observed on the San Andreas fault (Zoback et al., 1987). In the Black Butte well, orientations were found to vary up to  $30^{\circ}$  from the median NE direction for maximum compressive stress (Stock et al., 1986).

The most important conclusion that can be drawn from these apparently contradictory results is that local perturbations in a regional stress field are likely results of rheological heterogeneity and geometry. Therefore, in order to accurately define stress trajectories, a large number of measurements are required, sensing to different depths, and using a variety of techniques. Perhaps this is the best approach to understanding fault rheology along the San Andreas fault system.

CHAPTER 5  
CONCLUSIONS

Thermal effects dominate both the magnitude and orientation of stresses measured within 6 m of the surface in the two different rock types encountered in this study. At site LRS, a nearly exponential decay in stress magnitudes was observed during the summer to a depth of 6 m. The observed average stress profile was modeled using the one dimensional heat conduction equation applied to a thermally isotropic half space, heated from the surface by a sinusoidally varying annual temperature. Observed stress magnitudes are a factor of 2.7 larger than those predicted by the model, a discrepancy which is reconcilable by our uncertainty in Young's modulus, temperature and coefficient of thermal expansion for the rocks involved. Stresses measured in granite at sites ADB and RBT, during the summer of 1979 and winter of 1980 respectively, are consistent with the effects of seasonal temperature variations.

In situ stresses, measured by the U. S. Bureau of Mines strain relief method, have been shown to yield orientations for the maximum horizontal compressive stress which are consistent with other techniques sensing to greater depths. The assumption has been made, therefore, that NNW oriented in situ stresses measured below 6 m depth in this study are tectonic in origin. The existence of NNW

oriented residual stresses at site IMS cannot be dismissed, though it seems unlikely because the orientation is the same as that obtained in a different rock type at site LRS. The NNW orientation for maximum compressive stress near Palmdale is compatible with a far field NNE orientation, and right lateral shear strain, provided the San Andreas fault has some shear strength in this region. This is in contrast to the San Andreas in central California, where the fault has little or no shear strength. Local changes in the orientation of maximum compressive stress are evidence of the dependence of stress trajectories on fault rheology and geometry.

Stress magnitudes determined by this technique, on the other hand, are highly variable. Local changes in rock properties yield measurements which vary as much as a factor of three compared to neighboring ones. Interpretations of stress magnitude at depth are therefore not plausible. A major source of uncertainty lies in the assumptions required regarding rock properties used for data reduction. These include the choice of secant moduli to represent a non-linear process, and to a lesser extent the choice of plane stress versus plane strain assumptions for the outcrop setting. Secant moduli from depressurization in a biaxial chamber are likely to be appropriate for calculating stresses from individual overcore measurements, provided biaxial testing is done immediately upon removing

the core from the ground. This may serve to minimize "drying" and "aging" effects on the core, but there remains an uncertainty about the effects of strain relaxation on rock fabric itself. For these reasons, a modulus calculated from biaxial tests may not accurately represent the rock in situ.

In summary, this relatively inexpensive technique can be used to map tectonic stress trajectories provided at least three conditions are met. First, measurement sites must be selected to minimize the effects of topography on in situ stresses. Second, measurements must be made below the depth at which seasonal ambient temperature variations are significant. In the rock types sampled during this study, this depth was found to be approximately 6 m. Third, a large number of measurements must be made at a given site in order to average the effects of local rock heterogeneity on in situ stress.

## REFERENCES

- Birch, F., Compressibility; Elastic constants, in Handbook of Physical Constants, edited by S. P. Clark, Jr., pp. 97-173, Geol. Soc. of America Memoir 97, 1966.
- Boley, B. A. and J. H. Weiner, 1960. Theory of Thermal Stresses, 586 pp., John Wiley, New York, 1960.
- Carslaw, H. S. and J. C. Jaeger, Conduction of Heat in Solids, 2nd ed., 510 pp., Clarendon Press, London, 1959.
- Clark, B. R., Stress anomaly accompanying the 1979 Lytle Creek Earthquake: Implications for earthquake prediction, Science, 211, 51-53, 1980.
- Clark, S. P., Jr., Thermal conductivity, in Handbook of Physical Constants, edited by S. P. Clark, Jr., pp. 459-482, Geol. Soc. America Memoir 97, 1966.
- Dahlgren, J. P., M. L. Sbar, R. M. Richardson, T. Engelder, R. Plumb, and E. Bergman, In situ stress measurements near the San Andreas fault, Palmdale California, EOS, Trans. Am. Geophys. Un., 60, 947, 1979.
- Dahlgren, J. P., The influence of thermally induced stress upon near-surface stress data near the San Andreas fault, Palmdale, California, 81 pp., Univ. of Ariz. M. S. Prepublication Manuscript, Dept. Geosciences, 1980.
- Davis, J. C., Statistics and Data Analysis in Geology, 250 pp., John Wiley, New York, 1973.
- Dibblee, T. W., Jr., Areal geology of the Western Mojave desert, California, U. S. Geol. Surv. Prof. Pap. 522, 153 pp., 1967.
- Duvall, W. I., and J. A. Aggson, Least squares calculation of horizontal stress for more than three diametrical deformations in vertical boreholes, Bu. Mines RI 7894, 12 pp., 1979.
- Flaccus, C. E., R. M. Richardson, M. L. Sbar, T. Engelder, and D. Yale, Tectonic stress on the San Andreas fault from strain relief measurements. EOS Trans. Am. Geophys. Un., 1980.

- Flaccus, C. E., and R. M. Richardson, Influence of thermal stress on in situ stress measurements, EOS trans. Am. Geophys. Un., v. 62, 1048, 1981.
- Friedman, M., Residual elastic strain in rocks, Tectonophysics, 15, 297-330, 1972.
- Gladwin, M. T., R. L. Gwyther, R. Hart, M. Francis, and M. J. S. Johnston, Borehole tensor strain measurements in California, J. Geophys. Res., v. 92, pp. 7981-7988, 1987.
- Haas, C. J., Static stress-strain relationships, in Handbook of Physical Properties of Rocks and Minerals, edited by Y. S. Touloukian, W. R. Judd, and R. F. Roy, pp. 123-176, McGraw-Hill, New York, 1981.
- Harrison, J. C., Cavity and topographic effects in tilt and strain measurements, J. Geophys. Res., v. 81, pp. 319-328, 1976.
- Hooker, V. E., and W. I. Duvall, In situ rock temperature: Investigations in rock quarries, 1971., Bu. Mines RI 7589, 1971.
- Hooker, V. E., and D. L. Bickel, Overcoring equipment and techniques used in rock stress determinations, 32 pp., Bu. Mines IC 8618, 1974.
- Jaeger, J. C., and N. G. W. Cook, Fundamentals of Rock Mechanics, 515 pp., Chapman and Hill, London, 1969.
- Mabey, D. R., Gravity survey of the Western Mojave Desert, California, U. S. Geol. Surv. Prof. Pap. 316-D, 73 pp., 1960.
- Mardia, K. V., Statistics of Directional Data, 357 pp., Academic Press, London, 1972.
- McGarr, A., M. D. Zoback, and T. C. Hanks, Implications of an elastic analysis of in situ stress measurements near the San Andreas fault, J. Geophys. Res., v. 87, pp. 7797-7806, 1982.
- Mellor, J. W., Higher Mathematics, pp. 527-529, Dover Publications, Inc., New York, 1955.
- Merrill, R. H., and J. R. Peterson, Deformation of a borehole in rock, Bu. Mines RI 5881, 32 pp., 1961.

- Merrill, R. H., Three-component borehole deformations gage for determining the stress in rock, Bu. Mines RI 7015, 38 pp., 1967.
- NOAA, Climatological data for California, v. 82, Environmental Data Service, National Climatic Center, Asheville, North Carolina, 1978.
- NOAA, Climatological data for California, v. 83, Environmental Data Service, National Climatic Center, Asheville, North Carolina, 1979.
- NOAA, Climatological data for California, v. 84, Environmental Data Service, National Climatic Center, Asheville, North Carolina, 1980.
- Norman, C. E., Geometric relationship between geologic structure and ground stresses near Atlanta, Ga., Bu. Mines RI 7365, 24 pp., 1970.
- Obert, L., In situ determination of stress in rock, J. Mining Eng., v. 14, pp. 51-59, 1962.
- Plumb, R. A., and S. H. Hickman, Stress-induced borehole elongation: A comparison between the four-arm dipmeter and the borehole televiwer in the Auburn geothermal well, J. Geophys. Res., v. 90, pp. 5513-5521, 1985.
- Reik, G. A., and J. B. Currie, A study of relations between rock fabric and joints in sandstone, Can. J. Earth Sci., v. 11, pp. 1253-1268, 1974.
- Richardson, R. M., and E. A. Bergman, Finite element modeling of stress along the San Andreas fault, EOS Trans. Am. Geophys. Un., v. 60, 952-953, 1979.
- Roy, R. F., A. E. Beck, and Y. S. Touloukian, Thermophysical properties of rocks, in Physical Properties of Rocks and Minerals, edited by Y. S. Touloukian, W. R. Judd, and R. F. Roy, pp. 409-502, McGraw-Hill, New York, 1981.
- Saada, A. S., Elasticity theory and applications, 643 p., Pergamon Press, Inc., New York, 1974.
- Savage, J. C., and G. Gu, The 1979 Palmdale, California, strain event in retrospect, J. Geophys. Res., v. 90, pp. 10301-10309, 1985.

- Sbar, M. L., T. Engelder, R. Plumb, and S. Marshack, Stress pattern near the San Andreas fault, Palmdale, California, from near-surface in situ measurements, *J. Geophys. Res.*, v. 84, pp. 156-164, 1979.
- Sbar, M. L., and R. M. Richardson, Measurement and analysis of the near surface stress field in the vicinity of active faults in southern California, Final Technical Rpt., U. S. Geol. Survey Contract 14-08-0001-17705, 1981.
- Sbar, M. L., Stress domains in western North America and tectonic interpretation, *J. Geophys. Res.*, v. 87, 3919-3928, 1982.
- Sbar, M. L., R. M. Richardson, C. E. Flaccus, and T. Engelder, Near surface in situ stress, Part 1: Strain relaxation measurements and the San Andreas fault, *J. Geophys. Res.*, v. 84, pp. 9323-9332, 1984.
- Skinner, B. J., Thermal expansion, in *Handbook of Physical Constants*, edited by S. P. Clark, Geol. Soc. of America Memoir 97, pp. 75-96, 1966.
- Springer, J. E., Stress orientations from well bore breakouts in the Coalinga region, *Tectonics*, v. 6, pp. 667-676, 1987.
- Springer, J. E., and M. J. Alder, Televiewer data report for the test interval 6250-6935, Cajon Pass well, California, U. S. Geol. Survey Open File Rept. 87-290, 39 pp., 1987.
- Stock, J. E., J. H. Healy, and J. Svitek, Hydraulic fracturing stress measurements at Black Butte, Mojave desert, CA, *EOS Trans. Am. Geophys. Un.*, v. 67, no. 16, p. 382, 1986.
- Timoshenko, S. and J. M. Goodier, *Theory of Elasticity*, 2nd ed., 506 p., McGraw-Hill, New York, 1959.
- Tullis, T. E., Stress measurements via shallow over-coring near the San Andreas fault, in *Mechanical Behavior of Rocks*, edited by N. L. Carter, M. Friedman, J. M. Logan, and D. W. Stearns, *Amer. Geophys. Un. Mono.* 24, pp. 199-214, 1981.
- Walsh, J. B., The effect of cracks on the elastic compression of rocks, *J. Geophys. Res.*, v. 70, pp. 389-411, 1965.

- Walsh, J. B., Theoretical bounds for thermal expansion, specific heat, and strain energy due to internal stress, *J. Geophys. Res.*, v. 81, pp. 319-328, 1973.
- Witherspoon, P. A., N. G. A. Cook, and J. E. Gale, Geologic storage of radioactive waste: Field studies in Sweden, *Science*, v. 211, pp. 894-900, 1981.
- Zoback, M. D., D. Moos, L. Mastin, and R. N. Anderson, Well bore breakouts and in situ stress, *J. Geophys. Res.*, v. 90, pp. 5523-5530, 1985.
- Zoback, M. D., H. Tsukuhara, and S. Hickman, Stress measurements in the vicinity of the San Andreas fault: Implications for the magnitude of shear stress at depth, *J. Geophys. Res.*, Special Issue on Stress 5352, 1980.
- Zoback, M. D., M. L. Zoback, S. Mount, J. Suppe, J. P. Eaton, J. H. Healy, D. Oppenheimer, P. Reasenber, L. Jones, C. B. Raleigh, I. G. Wong, O. Scotti, and C. Wentworth, New evidence on the state of stress of the San Andreas fault system, *Science*, v. 238, pp. 1105-1111, 1987.